

# ***YJ-594: Candidate Engine for the Next Generation Supersonic Transport***

AIAA 2017 - 2018 Undergraduate Engine  
Design Competition

**Advisor:**  
Jerry Seitzman

**Team Leader:**  
Ted Vlady

**Team Members:**  
Rocktim Datta  
Santusht Sairam  
Steve Zakharov  
Hamdaan Jaleel



**Georgia** Institute  
of **Tech**nology®

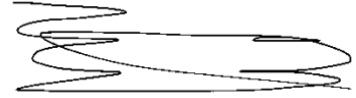
**SIGNATURE PAGE:**

Design Team:

Ted Vlady  
#921865



Steve Zakharov  
#921876



Rocktim Datta  
#921714



Santusht Sairam  
#922098



Hamdaan Jaleel  
#738418



Faculty Advisor  
Jerry Seitzman  
#070425

## Abstract

The YJ-594 is a two spool, mixed flow, variable cycle engine designed as a candidate for commercial supersonic flight in 2025. It features drastic fuel savings at all mission points coupled with an 8% decrease in engine weight and an extended mission range of approximately 4500 nautical miles. The YJ-594 engine's defining feature is its single bypass variable cycle engine architecture. Optimized turbomachinery, new composite materials and innovative technologies work together to minimize engine weight and noise and maximize range.

<b>General characteristics</b>	
Wing Area (in <sup>2</sup> )	4096.76
Max Take-off Weight (lbm)	317,499
Takeoff-Thrust (lbf)	64625
Design Afterburning Thrust	N/A
<b>Performance</b>	
Maximum Speed (MN)	1.8
Cruise Speed (MN)	1.6
Mission Fuel Burn (lbm/engine)	62257.9
Cruise TSFC (lbm/hr/lbf)	1.0324
Takeoff TSFC (lbm/hr/lbf)	0.4921
Engine Weight (lbm)	11870
Fan Diameter (in)	80.5
<b>Required Trade Studies</b>	
Aircraft Constraint Diagram Page #	2
Engine Cycle Design Space Carpet Plots Page #	9
In-Depth Cycle Summary Page #	13
Final engine Flow Path Page #	15
Final cycle study using chosen cycle program Page #	14
Detailed stage by stage turbomachinery design information Page #	Fan: 21      HPT: 34 HPC: 24      LPT: 36
Detailed design of velocity triangles for first stage of each component Page #	Fan: 22      HPT: 35 HPC: 25      LPT: 36
Detailed inlet and nozzle performance characteristics Page #	Inlet: 17      Nozzle: 43

1.	INTRODUCTION .....	1
2.	CONSTRAINT ANALYSIS .....	1
3.	MISSION ANALYSIS.....	3
4.	MODELING ENVIRONMENT.....	3
5.	CYCLE ANALYSIS.....	5
I.	DESIGN PROCESS .....	5
II.	ENGINE ARCHITECTURE DESIGN.....	5
III.	ENGINE ARCHITECTURE FINAL DESIGN: .....	6
IV.	CYCLE OPTIMIZATION.....	7
6.	ENGINE OPTIMIZATION USING A NEURAL NETWORK APPROACH.....	11
I.	TRAINING THE MODEL .....	11
II.	TEST DATA RESULTS .....	12
7.	IN DEPTH CYCLE SUMMARY.....	13
I.	FINAL CYCLE STUDY USING CHOSEN CYCLE PROGRAM .....	14
8.	INLET.....	15
I.	DESIGN.....	15
II.	INLET PERFORMANCE AND INLET FLOW STATION DATA.....	17
III.	FINAL INLET DESIGN .....	17
9.	COMPRESSORS.....	17
I.	COMPRESSOR DESIGN STRATEGY.....	17
II.	FAN .....	20
III.	HIGH PRESSURE COMPRESSOR.....	23
IV.	BLADE STRESS AND MATERIAL SELECTION .....	26
V.	BLADE AND DISK DESIGN.....	27
VI.	COMPRESSOR MAPS.....	28
VII.	FINAL COMPRESSOR ANALYSIS.....	28
10.	BURNER.....	29
I.	DESIGN.....	29
II.	NOX EMISSIONS .....	31
11.	TURBINES.....	32
I.	TURBINE DESIGN STRATEGY .....	32
I.	HIGH PRESSURE TURBINE .....	34
II.	LOW PRESSURE TURBINE .....	35
III.	BLADE STRESS AND MATERIAL SELECTION .....	36
IV.	FINAL TURBINE DESIGN .....	37
12.	VARIABLE CYCLE IMPLEMENTATION.....	38
I.	VARIABLE BYPASS DESIGN .....	38
II.	VABI MIXER.....	39
III.	EFFICIENCY .....	40
13.	NOZZLE .....	40
I.	DESIGN OF NOZZLE.....	40
II.	NOISE.....	41
III.	FINAL NOZZLE DESIGN.....	43
14.	CONCLUSION.....	44
	REFERENCES.....	46
	APPENDIX A: NPSS OUTPUT FILE DESIGN POINT YF-594 .....	48
	APPENDIX B: HAND CALCULATIONS FOR FIRST STAGE VELOCITY TRIANGLES OF TURBOMACHINERY.....	49

## List of Figures:

Figure 1: Aircraft Constraint Diagram at Takeoff .....	2
Figure 2: Baseline Model NPSS output .....	4
Figure 3: Final Engine Architecture .....	7
Figure 4: FPR vs. Cruise TSFC Carpet Plot .....	9
Figure 5: HPC vs. T4 vs. Cruise TSFC Carpet Plot.....	10
Figure 6: BPR vs. T4 vs. Cruise TSFC Carpet Plot.....	10
Figure 7: Neural network training error decrease (20-degree polynomial fit).....	12
Figure 8: Magnified Plot of the Neural Network error decrease (20-degree polynomial fit).....	12
Figure 9: Throttle Hook Performance YJ-594 .....	14
Figure 10: WATE++ 2D flow path YJ-594 .....	15
Figure 11: Diverterless Inlet F-35.....	16
Figure 12: Velocity Triangle Diagram Compressor .....	19
Figure 13: Velocity Triangles at the Hub, Mean and Tip for Fan .....	22
Figure 14: HPC velocity triangles at the Mean line.....	25
Figure 15: NACA Airfoil Selection chart.....	27
Figure 16: Blisk Design .....	28
Figure 17: Fan, Swan neck duct and HPC Sizing.....	29
Figure 18: RQL Design.....	30
Figure 19: Turbine Velocity Triangle Notation .....	32
Figure 20: Velocity Triangles at Mean line for HPT.....	35
Figure 21: Velocity Triangles at Mean line for LPT .....	36
Figure 22: AN <sup>2</sup> Typical Limits.....	37
Figure 23: HPT, Inter Turbine duct, LPT Initial Sizing .....	38
Figure 24: Proposed Noise Suppressor .....	43

## List of Tables:

Table 1: Aircraft Constraint Variables.....	2
Table 2: Mission Fuel Analysis .....	3
Table 3: VCE vs Baseline Architecture Fuel Comparison .....	7
Table 4: HPC Weight vs Mission Fuel .....	8
Table 5: FPR vs Weight vs Mission Fuel .....	9
Table 6: Epoch vs Error for the Neural Network.....	11
Table 7: Summary of Neural Network Values .....	13
Table 8: In-depth Cycle Summary .....	13
Table 9: Mission Fuel Comparison.....	15
Table 10: Inlet Type Design Study .....	16
Table 11: Inlet Flow Conditions .....	17
Table 12: Inlet Performance Characteristics .....	17
Table 13: Fan Inlet Conditions .....	20
Table 14: Initial Fan Design Values- Stage 1 .....	21
Table 15: Fan Design Values at Mean line.....	21
Table 16: HPC Flow Station Data .....	23
Table 17: HPC Design Values Stage 1 .....	23
Table 18: HPC Design Values at Mean line .....	24
Table 19: Blade Stress and Material Selection .....	26

Table 20: Burner Inlet Flow Conditions .....	29
Table 21: LTO Cycle Emissions Data .....	31
Table 22: HPT Inlet Flow conditions.....	34
Table 23: HPT Initial Design Choices .....	34
Table 24: HPT Design Values at Mean line .....	34
Table 25: Initial Design Choices LPT .....	35
Table 26: LPT Inlet Flow Conditions .....	35
Table 27: LPT Design Values at Mean line .....	36
Table 28: Blade Stress and Material Selection Turbine.....	37
Table 29: VABI Positioning Diagram .....	40
Table 30: Nozzle Inlet Flow Conditions .....	43
Table 31: Nozzle Performance.....	43
Table 32: Performance Requirements Matrix .....	44

### List of Equations

Equation 1: Climb Constraint .....	1
Equation 2: Turn constraint .....	1
Equation 3: Take off Constraint.....	1
Equation 4: Cruise Constraint .....	2
Equation 5: Landing Constraint .....	2
Equation 6: Shaft Speed.....	18
Equation 7: Inlet Area .....	18
Equation 8: Mean Speed relationship .....	18
Equation 9: Euler Turbine Equation .....	19
Equation 10: Stage pressure ratio .....	19
Equation 11: Exit Hub/ Tip.....	20
Equation 12: Isentropic Density Ratio .....	20
Equation 13: Adiabatic Temperature Relation .....	20
Equation 14: Specific Strength needed for Blade .....	26
Equation 15: Annulus Area.....	26
Equation 16: Production of NO <sub>x</sub> vs Fuel mixing ratio .....	30
Equation 17: NO <sub>x</sub> Emissions Equation .....	31
Equation 18: W <sub>theta3</sub> Calculation for Turbine.....	33
Equation 19: Specific Work of Stage.....	33
Equation 20: Power produced by Stage .....	33
Equation 21: Annulus Area.....	33
Equation 22: Blade Height.....	33
Equation 23: Poiseuille equation .....	39
Equation 24: Dominant Frequency .....	42

## List of Acronyms

T/W	Thrust to Weight Ratio
W/S	Wing Loading
RFP	Request for Proposal
NASA	National Aeronautics and Space Administration
DAL	Deceleration, Approach and Landing
NPSS	Numerical Propulsion Simulation Software
WATE	Weight Analysis for Turbine Engines
BPR	Bypass Ratio
FPR	Fan Pressure Ratio
T4	Turbine Inlet Temperature
TSFC	Thrust Specific Fuel Consumption
OPR	Overall Pressure Ratio
HPC	High Pressure Compressor
PR	Pressure Ratio
VCE	Variable Cycle Engine
ACE	Adaptive Cycle Engine
VABI	Variable Area Bypass Injector
BP	Bypass Duct
VC	Variable Cycle
RPM	Rotations Per Minute
CMC	Ceramic Matrix Composites
RQL	Rich-Burn, Quick-Mix, Lean-Burn
LTO	Landing Takeoff Cycle
HPT	High Pressure Turbine
LPT	Low Pressure Turbine
CFD	Computational Fluid Dynamics
MN	Mach number

## Acknowledgements

The design team would like to thank Dr. Seitzman for his invaluable suggestions to the design and spending time outside of the typical work day advising the team. Additionally, the team would like to thank Georgia Tech ASDL for their help and assistance on NPSS and WATE.

## 1. Introduction

It is necessary to conduct a preliminary constraint analysis and mission fuel analysis prior to engine design. These tests establish baseline values to constrain the engine design and assess opportunities for improvement.

## 2. Constraint Analysis

Dr. Andras Sobester's (University of Southampton) Jupyter notebook Python script is utilized to create a constraint diagram of thrust loading (T/W) verses wing loading (W/S) [1]. The process outlined in this code is directly sourced from his book, "Aircraft Aerodynamic Design." This process is elected over creating a custom excel sheet because of its higher quality visuals and ease of use. Equations and constants used to derive the constraint diagram are shown below. These values are taken directly from the RFP [2] and NASA supersonic aircraft report [3]. A few values, including the takeoff speed,  $C_L^{TO}$ ,  $C_D^{TO}$  and  $\mu_{TO}$  required extra research and the team ultimately decided to use past supersonic aircrafts for baseline values [4].

$\frac{T}{W} = \frac{V_V}{V} + \frac{q}{W/S} C_{Dmin} + k \frac{1}{q} \frac{W}{S}$ <p><i>Equation 1: Climb Constraint</i></p>	V <sub>v</sub> - rate of ascent- 5.7 m/s
	V- calibrated airspeed during climb- 128.6 m/s
	q- Dynamic pressure during climb- 9694.8 Pa
	C <sub>D min</sub> - minimum coefficient of drag- 0.019
	k-lift induced drag (calculated from Aspect ratio) - 0.097
$\frac{T}{W} = q \left[ \frac{C_{Dmin}}{W/S} + k \left( \frac{n}{q} \right)^2 \left( \frac{W}{S} \right) \right]$ <p><i>Equation 2: Turn constraint</i></p>	n-load factor-1.1
	q- dynamic pressure at cruise- 28082.2 Pa
	C <sub>D min</sub> - minimum coefficient of drag- 0.019
	k-lift induced drag (calculated from Aspect ratio) - .097
$\frac{T}{W} = \frac{V_L^2}{2g d_{GR}} + \frac{q C_D^{TO}}{W/S} + \mu_{TO} \left( 1 - \frac{q C_L^{TO}}{W/S} \right)$ <p><i>Equation 3: Take off Constraint</i></p>	V <sub>L</sub> - liftoff speed-113.2 m/s
	g-gravity constant- 9.81 m/s
	d <sub>GR</sub> - required ground run distance- 3048 m
	q- dynamic pressure at Takeoff- 3922.9 Pa
	C <sub>D</sub> <sup>TO</sup> - coefficient of drag at takeoff- 0.07
	C <sub>L</sub> <sup>TO</sup> - coefficient of lift at takeoff- 1.8
$\mu_{TO}$ - ground friction constant-0.04	



$\frac{T}{W} = q C_{Dmin} \frac{1}{W/S} + k \frac{1}{q} \frac{W}{S}$ <p><i>Equation 4: Cruise Constraint</i></p>	$C_{Dmin}$ - minimum coefficient of drag- 0.019
	q- dynamic pressure at cruise- 28082.2 Pa
	k-lift induced drag (calculated from Aspect ratio) - 0.097
$\frac{W}{S} \leq q^{APP} C_L^{APP}$ <p><i>Equation 5: Landing Constraint</i></p>	q- dynamic pressure at approach- 2158.1 Pa
	$C_L^{APP}$ - coefficient of lift at approach- 1.8

Table 1: Aircraft Constraint Variables

Below is the completed constraint diagram using the equations and formulas shown above. The optimum wing loading (W/S) and thrust to weight (T/W) for landing occurs at 0.25 T/W and 396.12 kg/m<sup>2</sup> or 81.1 psf W/S. This takeoff design point is show by the red triangle on the diagram. This value is very similar to the RFP wing loading value of 77.5 psf and given takeoff thrust over takeoff weight also known as thrust to weight ratio, validating the results of the constraint diagram.

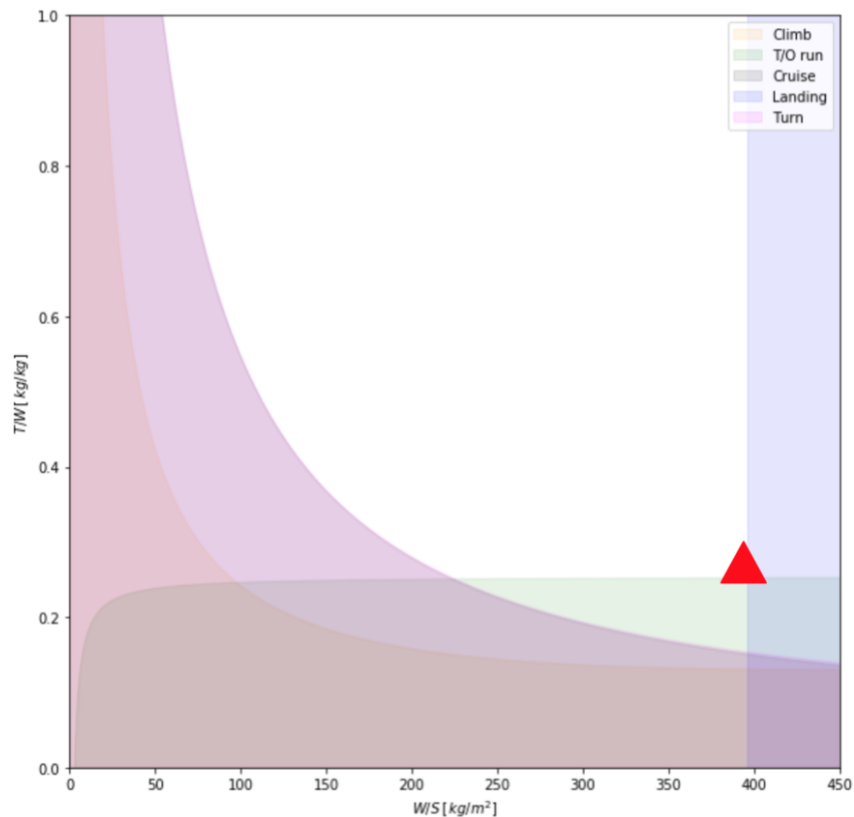


Figure 1: Aircraft Constraint Diagram at Takeoff

### 3. Mission Analysis

A mission flight profile is necessary to calculate fuel burn. The following table outlines such a profile.

Segment Name	Altitude(ft)	MN	Installed Thrust (lbf)	Time(hr)	Fuel Burned (lb)
Taxi Out	0	0	25850	0.15	2064.0
Takeoff	0	0	64625	0.0667	23435
Climb	20,000	0.85	28062	0.667	16315.7
Cruise	52,500	1.6	14685	2.84	45838
Deceleration, approach & landing	20,000	0.85	20267	0.333	6429.5

*Table 2: Mission Fuel Analysis*

Five major mission segments are outlined: taxi out, takeoff, climb, cruise and deceleration, approach and landing(DAL). The thrust values for takeoff and cruise match the RFP outline, while the thrust values for taxi out, climb and DAL were approximated to be 40%, 90% and 65% of max thrust at that speed and altitude, respectively. These values were predicted off the aircraft constraint diagram and then verified by comparing them to similar aircraft. Duration of most segments are outlined in the NASA supersonic aircraft report [3]. The cruise time is estimated to be 2.5 hours. This value is lower than anticipated, but acceptable considering the restrictions imposed on max takeoff weight of the proposed aircraft.

The total mission fuel burn for the baseline engine excluding reserves, is 67518.7 lbs. The aircraft carries 2 engines and has a max fuel capacity of 150,000 lb. of fuel, and allocates approximately 10% to reserves.

### 4. Modeling Environment

A combination of Numerical Propulsion Simulation Software (NPSS) [5] and Weight Analysis for Turbine Engines (WATE) [6] is used to model the thermodynamic cycle and calculate the weight and 2-D flowpath of the design. The combination of these two modeling environments provides an easy way to incorporate the output into an excel carpet plot template

as well as an easy way to manipulate the NPSS inputs. A custom script is used to conduct a ten by ten design space search of two independent variables and a dependent variable. This data is then input into an excel template and a carpet plot is generated.

The baseline engine is modeled in NPSS and WATE for preliminary design and baseline values [2]. A trade study script, excel carpet plot template and optimization algorithm is then used and validated with data from the baseline NPSS and WATE models. Below is the NPSS output file for the baseline engine. Additional information is included in the output file, which is truncated to only show performance and flow station data.

Summary Output Data													
MN	alt	dTamb	W	Fg	Fn	TSFC	BPR	VTAS	OPR	T4	T41	humRel	
1.600	52500.0	0.00	634.88	45498.5	15850.6	1.0211	1.91040	1582.49	36.813	3273.6	3150.1	0.000	
INSTALLED PERFORMANCE													
Wengine	Wbypass	Wbleed	Fram	FgIn	FnIn	TSFCin	eRam	Dinlet	Dnozz	Acapt	A0AC	Fan Diam	
615.58	0.0	19.30	29647.9	44318.1	14670.2	1.1032	0.9535	488.80	691.58	6767.15	0.8173	0.0000	
FLOW STATION DATA													
		W	Pt	Tt	FAR	ht	Wc	Ps	Ts	Aphy	MN	Rt	gamt
FS0	InEngStart.Fl_0	634.882	6.342	590.07	0.0000	141.09	1569.18	1.492	389.97	5714.9	1.6000	0.0686	1.39920
FS1	Inlet.Fl_0	615.583	6.047	590.07	0.0000	141.09	1595.71	5.081	561.48	6188.2	0.5049	0.0686	1.39920
FS2	IGVDuct.Fl_0	615.583	5.986	590.07	0.0000	141.09	1611.83	5.391	572.69	7630.3	0.3898	0.0686	1.39920
FS21	Fan.Fl_0	615.583	13.625	764.14	0.0000	183.10	805.93	12.240	741.34	3780.3	0.3950	0.0686	1.39366
FS13	Split.Fl_02	404.072	13.625	764.14	0.0000	183.10	529.02	12.203	740.71	2453.0	0.4006	0.0686	1.39366
FS23	Split.Fl_01	211.511	13.625	764.14	0.0000	183.10	276.92	11.991	737.04	1209.3	0.4318	0.0686	1.39366
FS25	SwanNeckDuct.Fl_0	211.511	13.488	764.14	0.0000	183.10	279.71	12.183	742.47	1340.6	0.3848	0.0686	1.39366
FS3	HPC.Fl_0	207.281	220.382	1768.17	0.0000	441.06	25.52	199.285	1723.77	123.2	0.3900	0.0686	1.33743
FS31	CDPBld.Fl_0	169.209	220.382	1768.17	0.0000	441.06	20.83	204.024	1734.05	112.7	0.3410	0.0686	1.33743
FS32	OGVDuct.Fl_0	169.209	217.120	1768.17	0.0000	441.06	21.15	211.678	1756.87	191.2	0.1951	0.0686	1.33743
FS4	BrnPri.Fl_0	173.705	211.670	3273.60	0.0266	904.57	30.30	210.332	3269.04	539.6	0.0995	0.0685	1.28233
FS45	HPT.Fl_0	208.604	36.590	2173.64	0.0220	567.75	171.52	33.090	2122.73	828.5	0.3946	0.0685	1.30714
FS48	ITTduct.Fl_0	208.604	36.590	2173.64	0.0220	567.75	171.52	33.090	2122.73	828.5	0.3946	0.0685	1.30714
FS5	LPT.Fl_0	213.892	13.080	1736.93	0.0215	442.43	439.79	11.795	1693.49	2100.9	0.3972	0.0685	1.32386
FS56	TEGVduct.Fl_0	213.892	12.949	1736.93	0.0215	442.43	444.23	12.412	1719.03	3154.4	0.2534	0.0685	1.32386
FS14	FanBld.Fl_0	404.072	13.625	764.14	0.0000	183.10	529.02	12.203	740.71	2453.0	0.4006	0.0686	1.39366
FS16	BPduct.Fl_0	404.072	12.943	764.14	0.0000	183.10	556.86	12.412	755.14	3966.0	0.2460	0.0686	1.39366
FS6	Mix.Fl_0	617.964	12.912	1120.76	0.0073	272.86	1033.90	12.342	1107.23	7120.4	0.2575	0.0686	1.36803
FS7	Tailpipe.Fl_0	617.964	12.847	1120.76	0.0073	272.86	1039.09	12.499	1112.49	9035.0	0.2009	0.0686	1.36803
FS9	NozPri.Fl_0	617.964	12.847	1120.76	0.0073	272.86	1039.09	1.492	616.55	5449.8	2.0581	0.0686	1.36803

Figure 2: Baseline Model NPSS output

The NPSS and WATE results are compared to the RFP [2] to confirm the validity of the modeling environment. While the NPSS model closely matches the output given in the RFP, the WATE model is 4% heavier than expected. This was determined to be an acceptable margin of error for an initial design.

It is worth noting that bypass ratio (BPR) or fan pressure ratio (FPR) are varied to maintain a total pressure ratio of 1 at the mixer during the initial design point analysis [7]. Thus, determining one value will set the other at design point. The biggest influencer of mission fuel

burn is turbine inlet temperature. In almost all cases, a turbine inlet temperature ( $T_4$ ) increase is received with a significant thrust specific fuel consumption (TSFC) decrease. Additionally, a FPR increase results engine weight reduction. This trend is attributed to the decrease in fan area and thus size when increasing FPR. Sacrificing a lower cruise TSFC in exchange for a lower engine weight is considered and thus further trade studies are required to determine the optimal trade-off point. Finally, the models indicate that increases in overall pressure ratio result in increased engine weight and lower fuel consumption. This trend is explored to determine an optimum high pressure compressor pressure ratio value.

## **5. Cycle Analysis**

### ***I. Design Process***

Literature on compressor pressure ratio ranges, maximum turbine inlet temperature and new engine architectures are considered to begin a cycle analysis and establish critical baseline parameters.

### ***II. Engine Architecture design***

Two primary engine architectures are analyzed. The first engine architecture is based on improving existing engine infrastructure by implementing composite materials and more efficient turbomachinery. The second architecture is the concept of a variable cycle engine (VCE).

The first design has advantages in its simplicity and weight savings compared to the VCE. However, little can be done to optimize the engine outside of supersonic cruise. Alternatively, the benefits of a VCE are significant during off design performance. GE Aviation claims their newest VCE has led to 25% fuel savings and a 35% increase in range [8]. These findings alone suggest a trade study is necessary to determine the optimum engine architecture.

The VCE allows for independent control of the fan operating line [9]. This feature is quite useful during off design performance of the engine and leads to the fuel savings mentioned.

Two possible VCE designs for the engine exist. The first is based on GE's new Adaptive Cycle Engine (ACE), which features two bypass streams [8], and the latter is a simpler VCE design containing only one bypass stream.

In the NPSS model, the addition of an outer stream adds many independent variables and complicates the optimization process. This design also uses the outer stream to take on spillage air. However, the supersonic commercial aircraft conducts most of its mission at supersonic cruise and the marginal improvements in reducing spillage drag do not outweigh the added weight of the full-length bypass duct associated with the third bypass stream. Essentially, the aircraft does not spend enough time at subsonic speeds, like Fighter Jets do, for the additional stream to exhibit considerable design improvements. The two-stream variable bypass design was ultimately scrapped due to modeling complexities and the marginal benefits of the third bypass stream.

The single bypass stream VCE is chosen and is compared against the baseline model. Initial pressure ratio values for fans and compressors are set and remain constant throughout the analysis. The bypass duct area is then varied to influence the BPR and fan operating line. This allows for the calculation of the optimum bypass duct area for each flight regime. Mission fuel weight savings greater than the additional weight of added components will validate the VCE's improvement over a baseline engine.

### ***III. Engine Architecture Final Design:***

NPSS testing determines the optimum BPR for each flight segment. This BPR is limited by the 1/2 the BP duct design point area, a fan stall margin of below 10% or a TSFC minimum.

The fuel per hour of the baseline model architecture and the VCE architecture, proposed for use on the candidate engine are compared below. Throttle is varied during the comparison to maintain constant thrust.

	Baseline architecture (lb fuel/hr)	VCE architecture (lb fuel/hr)	Fuel % saved
Transonic pitch	14177.52	13859.64	2.24
Climb/Descend point	24635.30	24459.69	0.71
Takeoff	35896	34587.18	3.65

Table 3: VCE vs Baseline Architecture Fuel Comparison

The data shows a substantial decrease in off design mission fuel burn. This translates to approximately 500 lbs. of fuel saved. Furthermore, there is a small increase in weight due to the VC architecture. This assumption is based off GE Aviation’s VCE engine, the YF120, only increasing engine weight by 10 lbs. [10]. Additionally, the VCE architecture weight additions are offset by the removal of the forced lobed mixer. As the results above show, the single variable bypass should be chosen for this competition due to its simplicity to model as well, its secondary purpose in reducing jet noise at cruise. Below is the final engine architecture.

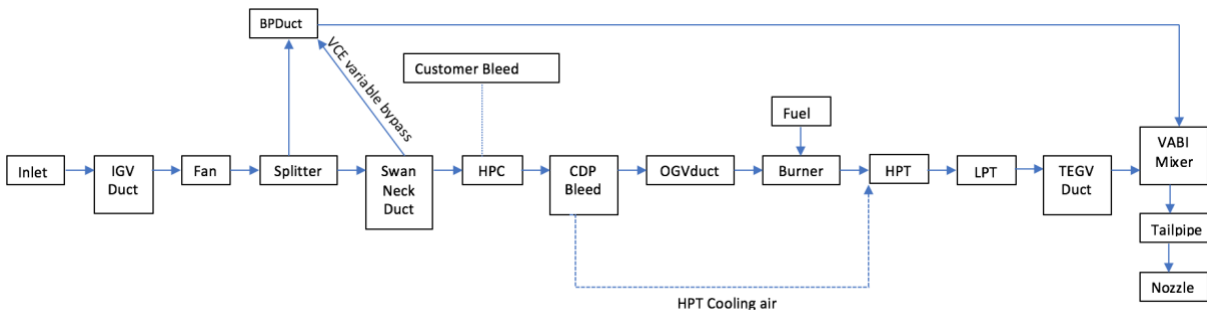


Figure 3: Final Engine Architecture

#### IV. Cycle Optimization

The initial model testing in conjunction with the VCE yield two changes: an altered turbine inlet temperature of 3350 °R and the removal of cooling air from all but the High-

Pressure Turbine entry. Due to the difficulty of modeling variable cycle architecture, the engine will be optimized without a variable cycle architecture at off design performance.

The OPR vs T4 trade study is used to determine the best possible OPR for a maximum range and validate the T4 assumptions made above. When collecting data, a baseline Fan PR of 2.5 and variable HPC PR is used. As the data below demonstrates, a HPC PR of approximately 23.5 optimizes range while higher values decrease mission fuel burn, albeit with diminishing returns. Lower OPR values decrease engine weight by removing stages from the HPC.

HPC PR	Engine weight	Engine Weight Gain	Mission Fuel	Fuel Weight Change	Net Loss or Gain
17	14700	N/A	64770	N/A	N/A
18	14736	36	64643	-127	-91
19	14774	38	64537	-106	-68
20	14792	18	64452	-85	-67
21	14850	58	64385	-67	-9
22	14886	36	64335	-50	-14
23	14911	25	64298	-37	-12
24	14968	57	64277	-21	36
25	15026	58	64266	-11	47

Table 4: HPC Weight vs Mission Fuel

A FPR vs BPR study is conducted next, with an emphasis on the engine weight and its impact on mission fuel weight. As the chart below shows, a FPR of 3.4 is the optimum point for maximizing range. However, the RFP requirements of 5% decrease in TSFC at takeoff result in a design choice of 2.57 FPR rather than the optimal, 3.2. This is due to the higher FPR decreasing inlet area and mass flow and lowering BPR, thus increasing fuel consumption at takeoff. This same phenomenon explains the decrease in engine weight as FPR is increased. The change in FPR decreases the necessary mass flow and hence the required inlet and fan size. Engine weight should significantly increase around a FPR of 2.7 due to the addition of a third stage.

FPR	Engine Weight (lb)	Weight Change (lb)	Mission Fuel (lb)	Fuel Weight change (lb)	Net Loss or Gain (lb)
2.2	19907	N/A	65534	N/A	N/A
2.3	18381	-1526	64989	-545	-2071

2.4	17130	-1251	64629	-360	-1611
2.5	16136	-994	64400	-229	-1223
2.6	15320	-816	64271	-129	-945
2.7	14677	-643	64155	-116	-759
2.8	14098	-579	64043	-112	-691
2.9	13611	-487	64095	52	-435
3.0	13200	-411	64197	102	-309
3.1	12841	-359	64350	153	-206
3.2	12515	-326	64532	182	-144
3.3	12228	-287	64721	189	-98
3.4	11985	-243	64960	239	-4
3.5	11842	-143	65231	271	128

Table 5: FPR vs Weight vs Mission Fuel

Using these two studies, the engine design parameters are set to design points that optimize aircraft range. Carpet plots and other similar counterparts for cruise TSFC trade studies outlined in the RFP are shown below.

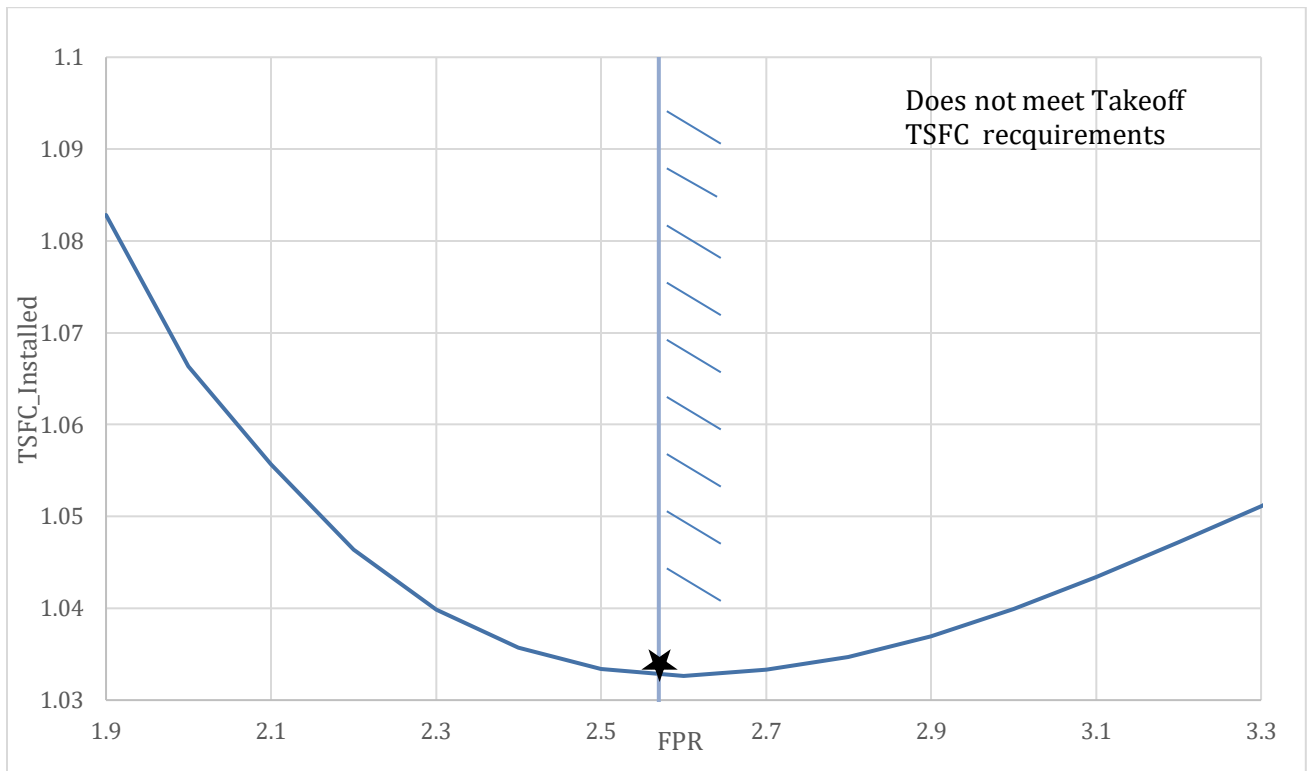


Figure 4: FPR vs. Cruise TSFC Carpet Plot



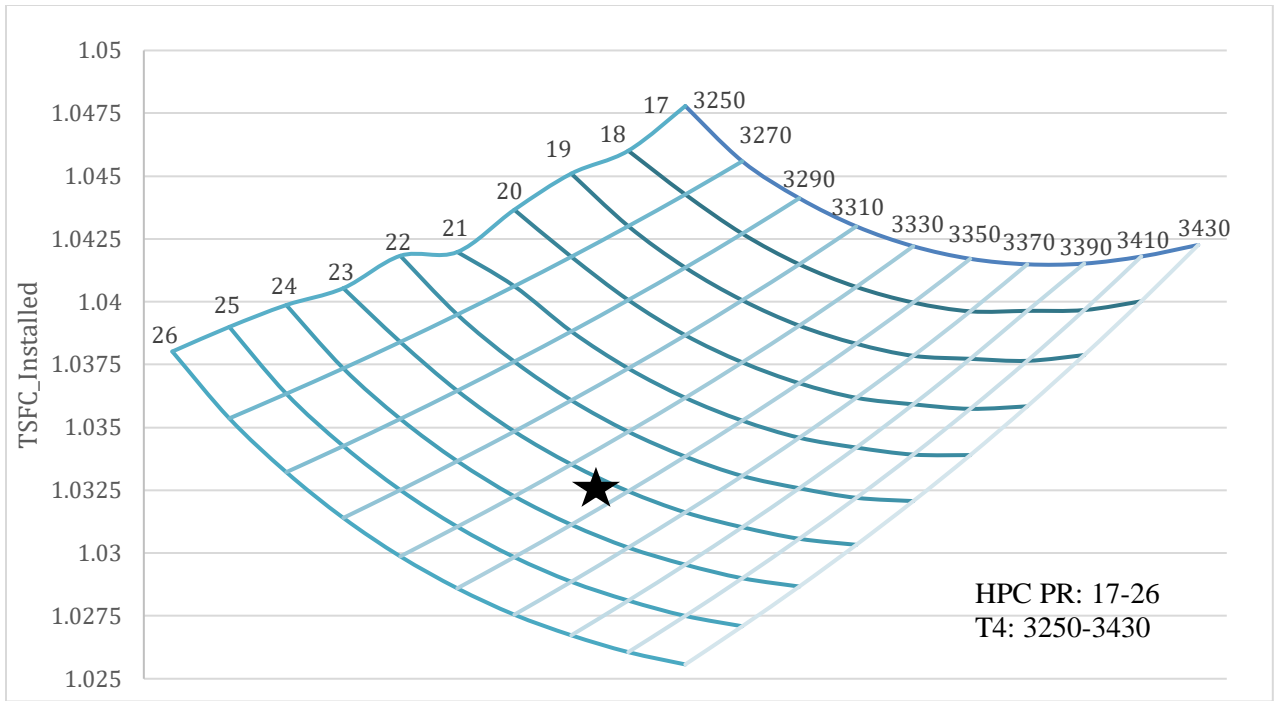


Figure 5: HPC vs. T4 vs. Cruise TSFC Carpet Plot

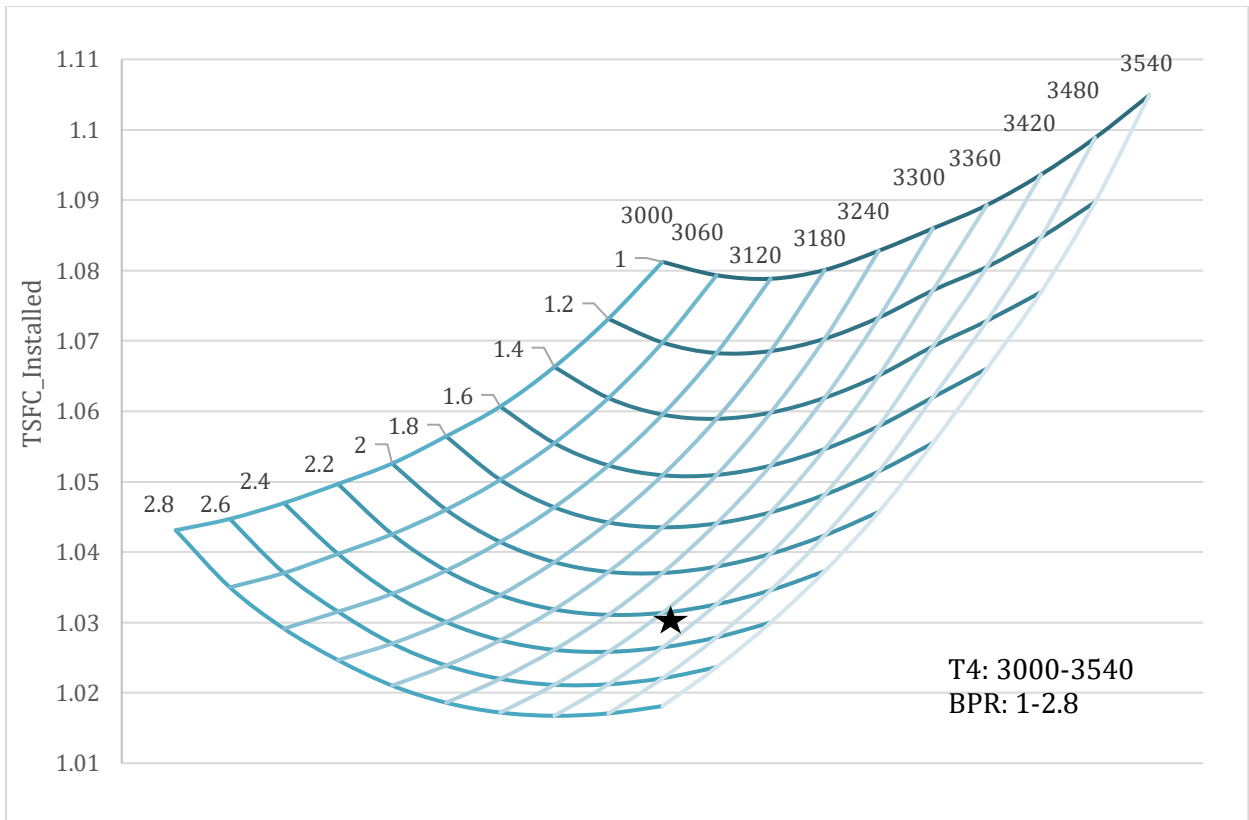


Figure 6: BPR vs. T4 vs. Cruise TSFC Carpet Plot

## 6. Engine optimization using a Neural Network approach

### I. Training the model

In addition to the method described above, pattern recognition via a neural network is employed to find an optimal design point for the engine specifications. It can be problematic to find points of minima for multi-dimensional functions with interdependent input parameters, and neural networks implement multi-layer collection of single decision-making units (perceptrons) to approximate a function that correlates input and output parameters (based on a training dataset).

Using NPSS, data is generated for each control variable to assess its impact on other parameters. Thus, a normalized dataset is generated for training. This ensures that the ratio of magnitudes of every perceptron's sum is equivalent to the ratio of the weight coefficients. The Multilayer Perceptron Neural Network is trained using various learning algorithms. A hyperbolic tangent activation function is used in tandem with a rectified linear function for the last layer.

The Neural Network implements the ADADELTA method, which calculates the gradient vectors based on first-order derivatives and adjusts learning rates for each individual weight coefficient. This gradient of the cost function is then multiplied by the learning rate and added to each weight. The gradient is backpropagated to previous layers and the process is repeated for each known data point. This brings the neural network's approximation closer to the function connecting input and output variables. Iterating over the dataset once completes one generation (epoch) of training.

The normalized dataset is shown to be consistent, containing no volatile parameters, and error as low as  $1.687e-07$  is achieved within 30 epochs with only 2 layers and 20 perceptrons.

Epoch	Error
1	5.57E-03
2	2.52E-04
3	4.98E-05
5	2.82E-05
10	3.26E-06
15	7.99E-07
20	5.04E-07
28	1.69E-07

Table 6: Epoch vs Error for the Neural Network

This illustrates that the approximation created by the neural network is essentially identical to the actual relationship between 7 input parameters and the output.

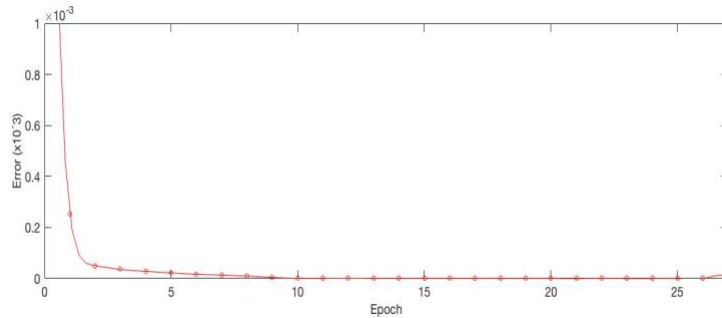


Figure 7: Neural network training error decrease (20-degree polynomial fit)

The bottom plot shows a magnified section of the plot with no approximations. The error decrease plot clearly contains discontinuities, which are present due to the training algorithm’s convergence on saddles while finding the global minimum of the cost function in a 6-D multivariable domain.

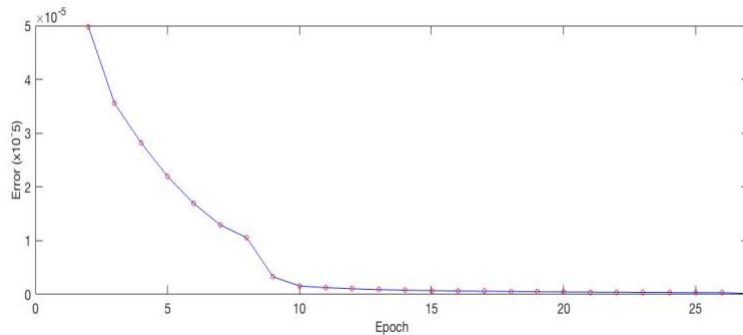


Figure 8: Magnified Plot of the Neural Network error decrease (20-degree polynomial fit)

## II. Test data results

A test dataset is created in accordance with the independent variables chosen: OPR (ranging between 40 and 65), FPR (ranging between 2-2.7) and T4 (ranging between 3200 and 3350). An optimal point where cruise TSFC is lowest is calculated upon data normalization and optimization. In a 3D data range, the lowest cruise TSFC is 1.03109 at an OPR of 65 and a T4 of 3350 (All other variables were held constant as shown in the table below).

	Fnet semi inst.	FPR	OPR	T4	Cruise TSFC
Real optimal values	15850	2.5	65	3350	1.03109
Normalized optimal values	0.46449	0.46825	0.50836	0.64803	0.16318
Train data range	15294 - 16491	0.48 - 4.80	31.7 - 97.2	3000- 3540	1.02 - 1.10
Test data range	15850	2.0-2.7	40-65	3200- 3350	-

Table 7: Summary of Neural Network Values

A higher T4 or OPR permits a lower cruise TSFC; however, those values require exceeding the domain of the engine specifications.

## 7. In depth Cycle Summary

While both approaches are effective in optimizing the engine, the first approach combining total mission fuel burn and engine weight is chosen. In the future, it is hoped the Neural Network approach can be applied to find the optimal range rather than the optimal cruise TSFC. Below are cycle summary parameters chosen in the first optimization method.

Summary Data	
Design MN	1.6
Design Altitude (ft)	52500
Design Fan Mass Flow (lbm/s)	587.690
Design Gross Thrust (lbf)	42980.4
Design Bypass Ratio	2.175
Design Net Thrust	14685
Design TSFC (lbm/hr/lbf)	1.0324
Design Overall Pressure Ratio	59.791
Design T4.1 (°R)	3350
Design Core Pressure Ratio	23.5
Design Fan / LPC Pressure Ratio	2.57
Design Chargeable Cooling Flow (% @25)	0%
Design Non-Chargeable Cooling Flow (% @25)	2.97%
Design Polytropic Efficiency for Each Compressor	Fan: 0.9, HPC: 0.9
Design Adiabatic Efficiency for Each Turbine	HPT: 0.91, LPT 0.91
Design HP & LP Shaft RPM	LP shaft: 4949, HP shaft: 12710
Design HP/LP Shaft Off-take Power Design	1% customer bleed
Customer Bleed Flow	100 HP Off-Take from HP shaft

Table 8: In-depth Cycle Summary

### I. Final cycle study using chosen cycle program

Below are the Installed Thrust vs. Installed TSFC curves and the RFP design points. The plot includes working variable cycle architecture described in a section above. As the carpet plot shows, the optimal FPR and bypass ratio is not chosen for the design point due to weight savings. Thus, the variable cycle architecture is active during cruise allowing for the best combination of weight and mission fuel saving. It is worth noting the candidate engine meets all the TSFC and Thrust requirements in the RFP without the Variable Cycle active.

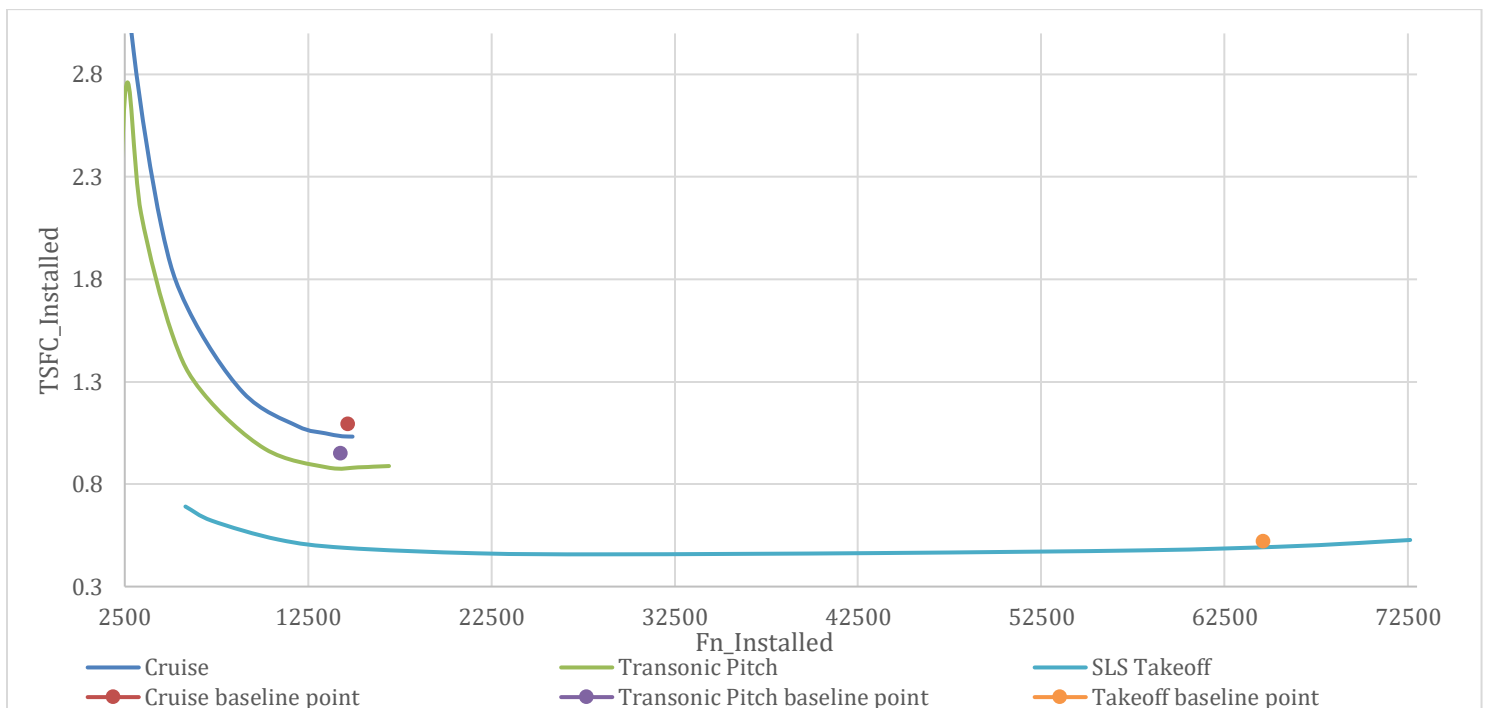


Figure 9: Throttle Hook Performance YJ-594

A mission fuel analysis is conducted following a confirmation of the candidate engine's ability to meet thrust and TSFC requirements in the RFP.

Segment Name	Fuel Burned (lb) Baseline Engine	Fuel Burned (lb) YJ-594 engine	Percent Change
Taxi Out	2064.0	1812.4	12.19%
Takeoff	2343.5	2121.81	9.46%
Climb	16315.7	14624.2	10.37%
Cruise	40365.7	37879.4	6.16%

Deceleration, approach & landing	6429.5	5820.12	9.48%
Total	67518.4	62257.9	7.79%

Table 9: Mission Fuel Comparison

The implementation of the VCE architecture leads to significant fuel savings at off design points such as climb and descent. Overall, the candidate engine saves 5261 lbs. of fuel, which can increase range by approximately 400 nautical miles.

Below, the final 2D flow path of the candidate engine is included. The yellow represents the framing that attaches the core to the nacelle. The VCE additions were unable to be modeled in the 2D flowpath due limitations from WATE.

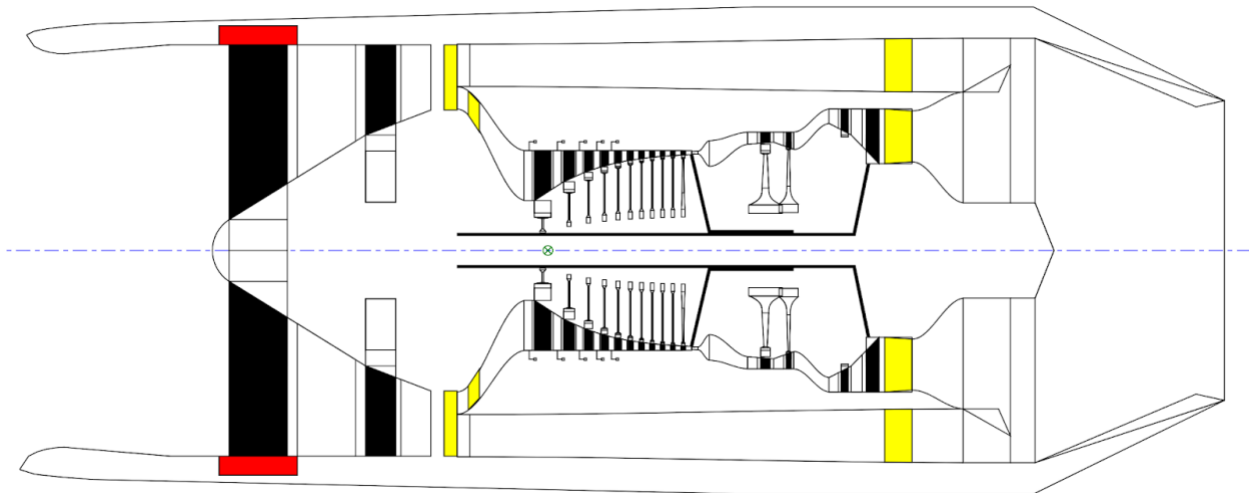


Figure 10: WATE++ 2D flow path YJ-594

## 8. Inlet

### I. Design

The options for a high-speed inlet are the variable spike intake, variable ramp intake, and diverterless intake. Factors such as weight, size, pressure losses and reliability are examined when selecting the optimal inlet design.

The variable spike intake, used in the SR-71, is lightweight, simple to manufacture and easily adjusts to changing speeds; however, it requires long ducting and suffers high efficiency

drops during climb and decent. Furthermore, the SR-71 inlets have been documented to fail during flight. Lastly, the spike inlet works best at high Mach numbers approaching hypersonic speeds, beyond the operating range of the candidate aircraft [11].

The ramped inlet, used in the F-15, can be adjusted to achieve optimum efficiency during all parts of the flight but is bulky and difficult to design and manufacture. Additionally, its complexity results in longer repair times, which is unideal for commercial aircrafts. [12].

Finally, the diverterless inlet is fairly new design by Lockheed Martin implemented in the F-35 fighter jet. A bump at the entrance of the inlet causes an oblique shock which diverts the boundary layer around the intake. Furthermore, the bump features several pinholes which act as a passive bleed system for the intake [26].

The main disadvantage of the diverterless inlet is the fact engine must be mounted such that the bump is integrated into the fuselage. However, NASA N+2 supersonic concept report details many supersonic commercial aircraft designs viable with this adjustment [3].



Figure 11: Diverterless Inlet F-35[26]

Inlet type	Weight	Length	Reliability	Efficiency across mission	Total
Variable spike	1	0	0	0	1
Variable ramped	0	1	1	1	3
Diverterless Inlet	1	1	1	1	4

Table 10: Inlet Type Design Study

Based on the information above, a trade study chart is created and used to decide which the optimal inlet. Results confirm the diverterless inlet as the ideal choice.

## II. Inlet Performance and Inlet Flow Station Data

Inlet Drags and inlet performance are modeled in accordance with suggestions outlined in the RFP. Due to chosen design values less engine airflow is needed at design point. The inlet must thus have a size of 6481 in<sup>2</sup>. This inlet size is about 5% smaller than the baseline model, which in turn allows for lower drags during all flight segments. The performance values, drag, bleed and bypass requirements for the engine at different segments of the mission are outlined in Table 12.

Mass flow (lb)	606.917
Corrected mass flow (lbm)	1500.06
Inlet Pt (psi)	6.342
Inlet Tt (R°)	590.07
Inlet FAR	0.0
Inlet MN	1.6
Inlet Area (in <sup>2</sup> )	5463.2
Pressure Change	0.9535

Table 11: Inlet Flow Conditions

Segment	Inlet mass flow	W_Bleed	W_Bypass	eRam	Drag (lbf)
Cruise	606.557	18.87	0.0	0.9535	453
Transonic Pitch	595.267	16.75	37.82	0.9670	1413
Takeoff	2084.153	0.0	0.0	0.9500	0.0

Table 12: Inlet Performance Characteristics

## III. Final Inlet Design

In the case of the inlet, as well as most of the cold sections of the engine, Ceramic matrix composites (CMC) are not needed. Instead, the inlet is manufactured using cheaper carbon fiber composites. Automated tape layup or automated fiber placement can be used to further drive down long-term costs. Integration with the airframe manufacturer can allow for even further savings down the road.

## 9. Compressors

### I. Compressor Design Strategy

Compressor design involves determining several engine parameters, including number of stages and blade design, which directly relate to engine weight. The compressors are designed using a repeated stage model for simplicity.



To begin design, a shaft speed is first determined. This is done by limiting the max tip Mach number to a design value and choosing a hub to tip ratio. Using Equation 7, the values for the first stage blade radii at hub, mean and tip can be found. A shaft speed is then calculated using Equation 6.

$$\vec{U} = \omega r \hat{e}_\theta$$

*Equation 6: Shaft Speed*

$$A_1 = \pi * r_{t1}^2 * \left[ 1 - \left( \frac{r_{h1}}{r_{t1}} \right)^2 \right]$$

*Equation 7: Inlet Area*

Following this design choice, a de Haller number is chosen. A minimum required value of .72 is chosen for the first stage, and subsequently increased to .75 as recommended by Farokhi [13]. The axial velocity ( $C_z$ ) is maintained constant throughout the entire compressor. Additionally, the repeating stage constraint requires the exit velocity and angle of each stage to match the entrance conditions of the next. As recommended by many textbooks, a mean line analysis is chosen for blade design [14].

Below is the diagram for a single stage and its respective velocity triangles. The relative and absolute velocities are calculated using simple geometric relationships as well as fact that:

$$U = W_\theta + C_\theta$$

*Equation 8: Mean Speed relationship*

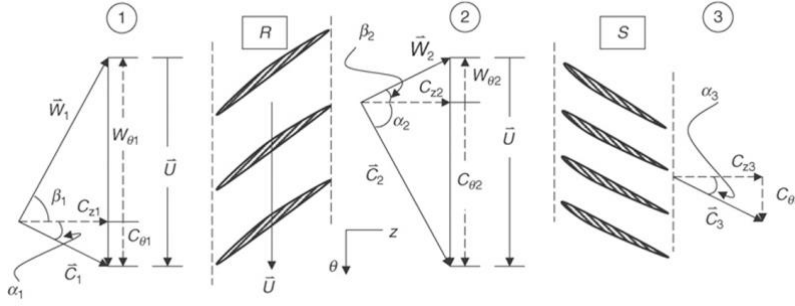


Figure 12: Velocity Triangle Diagram Compressor [13]

Velocity triangles for the hub at tip are calculated using the free stream velocity constraint.

This requires  $C_\theta * r$  to remain constant across the entire blade.

Following the determination of these velocities, loading, flow and work coefficients, as well as diffusion factors are determined and their compliance to standard values verified. Blade and stator solidity are chosen to maintain diffusion factor requirements.

The next step of the process is to determine the stage pressure ratio. This is done by finding the ratio of total pressure at the rotor exit over rotor entrance. Total Temperature at rotor exit is determined using the Euler Turbine equation shown below.

$$T_{t2,m} = T_{t1} - U_m * (C_{\theta 2} - C_{\theta 1}) / c_p$$

Equation 9: Euler Turbine Equation

Following the calculation of the total temperature ratio and the change in total temperature, the approximate number of stages as well as the stage total pressure is calculated. The approximate number of stages is simply the total temperature rise of the compressor divided by the total temperature rise of the stage. The calculation for the stage pressure ratio is shown below.

$$\pi_s = \tau_s^{\frac{\gamma \cdot e_c}{\gamma - 1}}$$

Equation 10: Stage pressure ratio

The final step of compressor design is to determine exit area conditions and thus the exit hub to tip ratios. Shown in the equations below, the new hub to tip ratio is derived by finding the relationship of the densities, which in turn are calculated through isentropic relationships.

$$\frac{r_{h2}}{r_t} = \sqrt{1 - \frac{\rho_1}{\rho_2} \left[ 1 - \left( \frac{r_{h1}}{r_t} \right)^2 \right]}$$

Equation 11: Exit Hub/ Tip

$$\frac{\rho_2}{\rho_1} = \left( \frac{T_2}{T_1} \right)^{\frac{1-\gamma(1-e_c)}{\gamma-1}}$$

Equation 12: Isentropic Density Ratio

$$T = T_t - C^2/2c_p$$

Equation 13: Adiabatic Temperature Relation

Using the process outlined above, an excel sheet capable of calculating compressor using only 8 inputs from NPSS and 6 design variables is developed. The sections below outline the design choices for the fan and high-pressure compressor.

## II. Fan

Basic fan inlet conditions and some compressor parameters required to initialize design are listed in table 13. The FPR for the proposed fan is slightly higher than the baseline model. To compensate for this, a higher max tip speed of 1.5 Mach is chosen.

Mass flow (lb)	588.434
Corrected mass flow (lbm)	1540.74
Inlet Pt (psi)	5.986
Inlet Tt (R°)	590.07
Inlet FAR	0.0
Inlet MN	0.3898
Inlet Area (in <sup>2</sup> )	7293.8
Pressure rise across fan	2.570

This leads to a low-pressure shaft speed of 4949 RPM. Relatively low de Haller numbers of 0.72 for the first stage and 0.73 for the second stage are chosen to optimize stage pressure ratios. Finally, a hub to tip ratio of 0.55 is selected for the first stage to achieve the higher pressure ratios necessary for compressor functionality. This in turn allows for a lower fan

diameter of 80.5 inches—an 8% decrease from the baseline model. Finally, solidities for the stator and rotor are chosen based on the Lieblein Diffusion Factor and aspect ratios of 1.5 are chosen for both the stator and rotor as recommended by Farokhi [13].

To the right is a chart of the design choices for the first stage of the fan. A constant tip radius is used for the fan compressor. After inputting the design values alongside fan entry values, other necessary parameters for velocity triangle calculations are obtained.

Max Tip Mach	1.5
$\sigma$ rotor solidity	1
$\sigma$ stator solidity	1.4
Hub to tip ratio	0.55
De Haller	0.72
Alpha1	0
Aspect Ratio	1.5
Polytropic efficiency	0.9

These design choices achieve the desired pressure ratio and temperature ratios in two stages. Additionally, major compressor values for both stages are outlined and velocity triangles for the hub mean and tip are calculated using the free stream velocity method. Blade design is considered in a following section.

Table 14: Initial Fan Design Values- Stage 1

Fan Stage	1		2	
	Rotor	Stator	Rotor	Stator
Lieblein Diffusion Factor	0.50	0.52	0.47	0.54
De Haller Number	0.72		0.73	
Stage Pressure Ratio	1.61		1.60	
Work Coefficient	0.32		0.30	
Flow Coefficient	0.34		0.30	
Hub-to-Tip Ratio	0.55	0.69	0.71	0.79
Mean radius(in)	31.19	33.99	34.36	36.00
Number of Blades	16	26	28	40
Aspect Ratio	1.50	1.50	1.5	1.50
Taper Ratio	0.8		0.8	
Tip Speed (ft/s)	1737.95		1737.95	
Stagger Angle	63.28	52.98	65.43	56.76
Blade chord	12.07	8.34	7.85	5.65
Degree of Reaction	0.84		0.85	
MN absolute	0.39	0.53	0.36	0.50
MN Relative	1.21	0.87	1.23	0.89

Table 15: Fan Design Values at Mean line

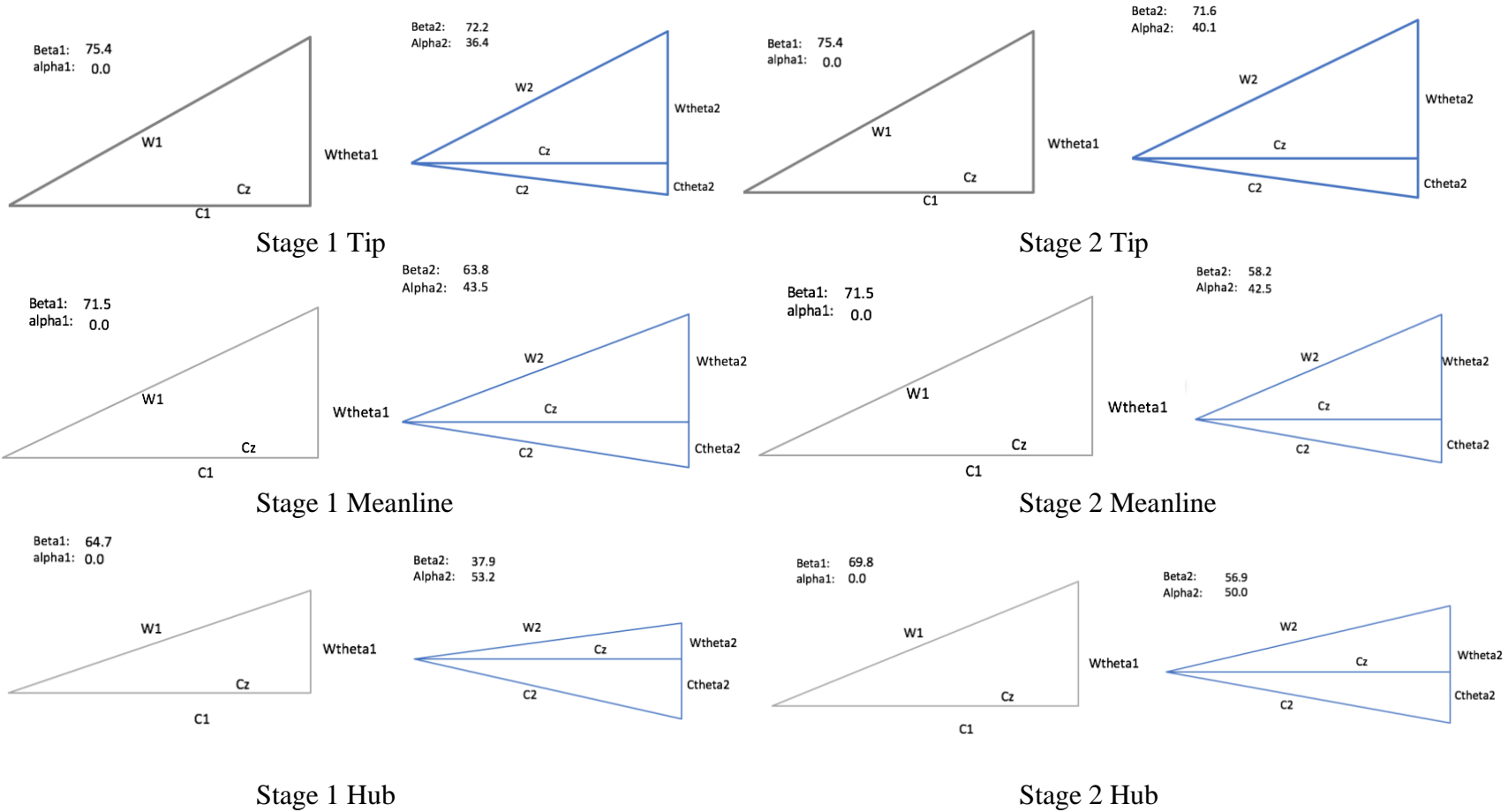


Figure 13: Velocity Triangles at the Hub, Mean and Tip for Fan

### III. High Pressure Compressor

The high-pressure compressor is designed using the same methods listed above. Its pressure ratio of 23.5 is significantly higher than the baseline engine. Additional research confirms the viability of this compressor, since an 11 stage, 27 pressure ratio HPC has already been used on the GE9x [18]. This suggests a highly efficient 11 stage 23 pressure ratio HPC will be viable for service in 2025.

Mass flow (lb/s)	185.333
Corrected mass flow (lbm)	221.14
Inlet Pt (psi)	15.231
Inlet Tt (R°)	793.27
Inlet FAR	0.0
Inlet MN	0.3848
Inlet Area (in <sup>2</sup> )	1060.2
Pressure rise across HPC	23.5

Table 16: HPC Flow Station Data

Following the same design process of the Fan, inlet conditions are listed to the right. A constant tip radius is maintained for the HPC. A tip Mach Number of 1.3 is necessary to achieve this pressure ratio, which translates to a high-pressure shaft speed of roughly 12700 RPM. A lower hub to tip ratio is required at the entrance to ensure that blade size at the exit is adequate. The de Haller number at the first stage is

Max Tip Mach	1.3
$\sigma$ rotor solidity	1.2
$\sigma$ stator solidity	1.5
Hub to tip ratio	0.5
De Haller	0.72
Alpha1	5.0
Aspect Ratio	2.0
Polytropic efficiency	0.9

Table 17: HPC Design Values Stage 1

0.72 and then rises to 0.74 in subsequent stages. Both design choices lie within the constraints laid out by Farokhi [13]. Solidity is again held constant throughout the compressor while still maintaining diffusion factor limits. Finally, aspect ratio for the stator and rotor begin at 2 and decrease as stage count increases to maintain minimum chord requirements. Below are the major parameters and velocity triangles at the mean line.

Compressor Stage	1		2		3		4		5		6	
	Rotor	Stator	Rotor	Stator	Rotor	Stator	Rotor	Stator	Rotor	Stator	Rotor	Stator
Lieblein Diffusion Factor	0.48	0.47	0.44	0.46	0.44	0.48	0.43	0.49	0.43	0.50	0.43	0.51
De Haller Number	0.72		0.74		0.74		0.74		0.74		0.74	
Stage Pressure Ratio	1.43		1.41		1.41		1.39		1.36		1.34	
Work Coefficient	0.36		0.33		0.32		0.32		0.31		0.31	
Flow Coefficient	0.39		0.36		0.34		0.33		0.32		0.32	
Hub-to-Tip Ratio	0.50	0.62	0.65	0.72	0.74	0.79	0.80	0.84	0.84	0.87	0.88	0.90
Mean radius(in)	11.93	12.91	13.09	13.70	13.81	14.24	14.32	14.62	14.67	14.89	14.93	15.09
Number of Blades	18	27	28	35	38	43	50	49	62	55	76	58
Aspect Ratio	2	2	1.92	1.8	1.84	1.6	1.76	1.4	1.68	1.2	1.6	1
Taper Ratio	0.8		0.8		0.8		0.8		0.8		0.8	
Tip Speed (ft/s)	1764.62		1764.62		1764.62		1764.62		1764.62		1764.62	
Stagger Angle	59.23	49.76	61.40	53.70	62.60	55.30	63.45	56.45	63.95	57.15	64.30	57.60
Blade chord	3.98	3.00	2.94	2.45	2.28	2.09	1.81	1.85	1.47	1.70	1.23	1.64
Degree of Reaction	0.80		0.82		0.82		0.83		0.83		0.83	
MN absolute	0.38	0.52	0.36	0.49	0.34	0.47	0.32	0.45	0.31	0.43	0.29	0.41
MN Relative	1.02	0.73	1.04	0.77	1.03	0.76	1.01	0.75	0.98	0.73	0.95	0.70

Compressor Stage	7		8		9		10		11	
	Rotor	Stator	Rotor	Stator	Rotor	Stator	Rotor	Stator	Rotor	Stator
Lieblein Diffusion Factor	0.43	0.51	0.43	0.51	0.43	0.52	0.43	0.52	0.43	0.52
De Haller Number	0.74		0.74		0.74		0.74		0.74	
Stage Pressure Ratio	1.31		1.29		1.27		1.25		1.23	
Work Coefficient	0.31		0.31		0.31		0.31		0.31	
Flow Coefficient	0.31		0.31		0.31		0.30		0.30	
Hub-to-Tip Ratio	0.90	0.92	0.92	0.93	0.93	0.94	0.94	0.95	0.95	0.96
Mean radius(in)	15.12	15.24	15.26	15.35	15.37	15.44	15.45	15.51	15.52	15.56
Number of Blades	91	71	106	86	121	103	135	121	149	142
Aspect Ratio	1.52	1	1.44	1	1.36	1	1.28	1	1.2	1
Taper Ratio	0.8		0.8		0.8		0.8		0.8	
Tip Speed (ft/s)	1764.62		1764.62		1764.62		1764.62		1764.62	
Stagger Angle	64.55	57.95	64.80	58.30	64.90	58.40	65.05	58.40	65.15	58.65
Blade chord	1.04	1.34	0.90	1.12	0.80	0.94	0.71	0.80	0.65	0.69
Degree of Reaction	0.83		0.83		0.83		0.83		0.83	
MN absolute	0.28	0.40	0.27	0.38	0.26	0.37	0.25	0.35	0.24	0.34
MN Relative	0.91	0.68	0.88	0.65	0.85	0.63	0.83	0.61	0.80	0.59

Table 18: HPC Design Values at Mean line

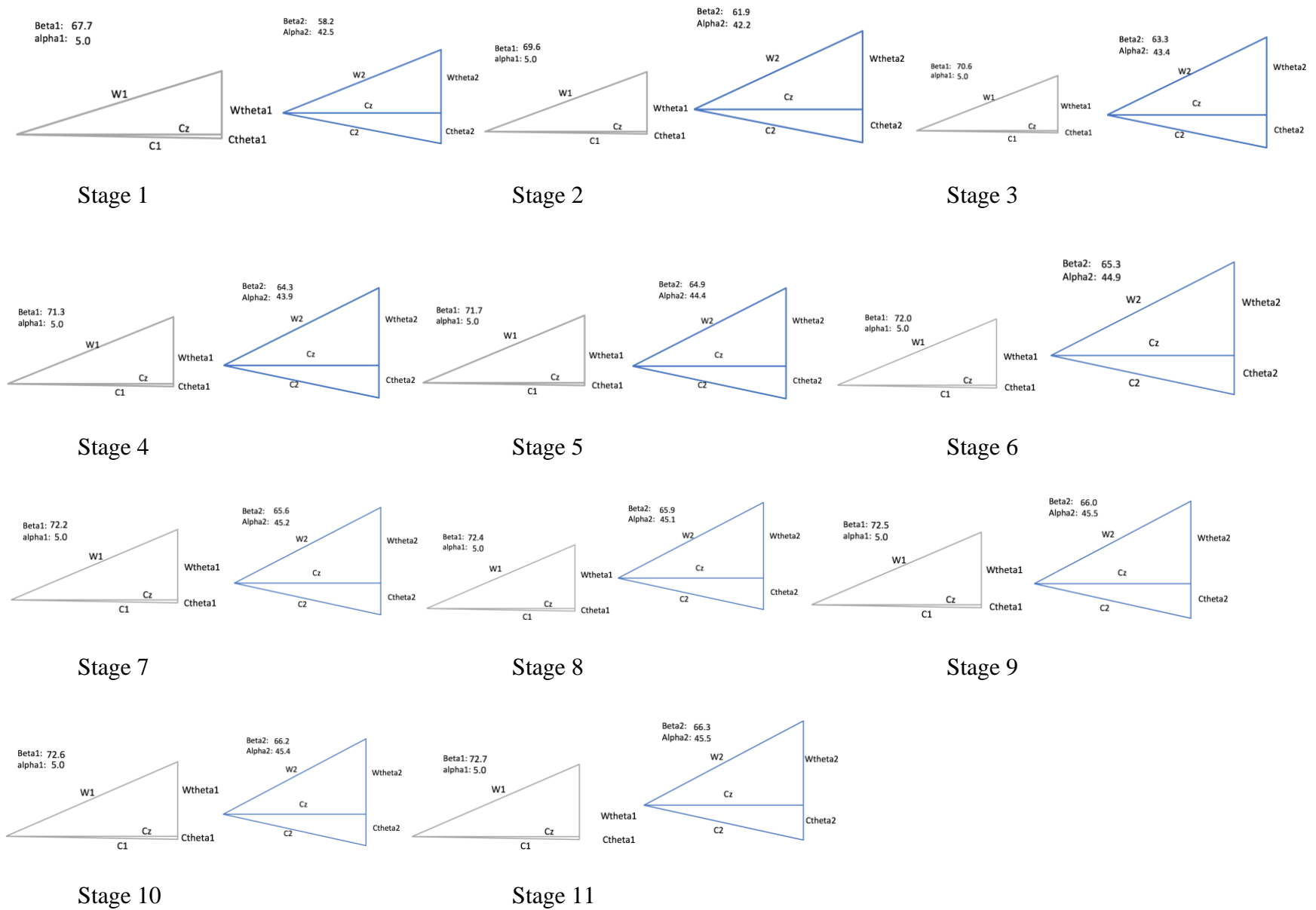


Figure 14: HPC velocity triangles at the Mean line



#### IV. Blade stress and Material selection

The next step in designing the compressors is blade and disk stress analysis and material selection. The temperature range across the compressor and the centrifugal stresses are first considered. These two factors are critical in determining manufacturing material. The fan operates at a relatively low temperature range between 600 °R and 800 °R, whereas the HPC operates at higher temperatures between 800 °R and 2000 °R.

The specific strength of each blade is calculated using the formula outlined below. Omega is obtained from the analysis carried out above, while area is estimated through Equation 15. Finally,  $A_t/A_h$  represents the taper ratio, which is chosen to be 0.8 throughout both compressors.

$$\frac{\sigma_c}{\rho_{blade}} = \frac{\omega^2 A}{4\pi} \left(1 + \frac{A_t}{A_h}\right)$$

Equation 14: Specific Strength needed for Blade

$$A = 2\pi * r_m * (r_t - r_h)$$

Equation 15: Annulus Area

It is worth noting the specific strength needed throughout the Fan or HPC decreases as the stage increases. Finally, a positive safety factor is maintained throughout when calculating the specific strength needed.

	Fan Stage 1	HPC stage 1	HPC stage 7
Inlet Tt (°R)	590	793	1484
Specific strength required (ft <sup>2</sup> /s <sup>2</sup> )	948046	1050941	265463
Material Chosen	Carbon Fiber, Steel leading edge	Titanium	Ceramic Matrix Composites (CMC)

Table 19: Blade Stress and Material Selection

A light, cheap, carbon fiber composite material with steel leading edges for the fan blades is used. The carbon fiber composite material has high specific strength and is suitable for the fan

blades. Carbon fiber composite allows for a light, strong blade with a high safety factor to prevent fractures. Steel leading edges protect the engine from foreign object ingestion. They are preferred over titanium due to their capacity for thinner blades and performance maximization [15].

Titanium alloy is used for the first six stages of the HPC due to its low relative cost and high specific strength. Finally, stages 7 through 11 of the HPC use CMC for its low density compared and high operating temperatures. Material changes, specifically to the fan and final stages of the HPC provide significant weight savings.

### V. *Blade and Disk design*

The final part of compressor design includes blade and disk design. Blade design relies primarily on flow speed and blade angles in determining a suitable airfoil. Because the relative airflow at the mean line is supersonic or transonic for almost all rotor stages, a Double Circular arc blade is chosen. The stator relative airflow is subsonic and hence a NACA blade is chosen using the chart on Figure 15.

Next, a disk type is chosen. A traditional disk with the blades attached by bolts is utilized, allowing for simple maintenance and replacement of fan blades. Additionally, it is impractical to manufacture a fan blisk due to its size. A ring disk type is recommended to achieve maintain stress requirements [16].

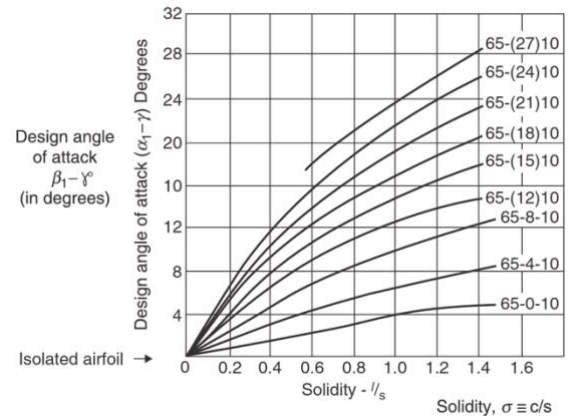


Figure 15: NACA Airfoil Selection chart [13]

Blisks however, are utilized for high pressure compressor design. Proven by CFM International, the blisk design can significantly decrease compressor weight. Shown in Figure 16, the blisk integrates the disk and blades into a single part. With the advent of additive manufacturing, these blisks are simple to create [17]. A ring type disk is used for the first stage due to stress conditions, followed by a web shape on later stages to save weight and maintain stress requirements [16].



*Figure 16: Blisk Design [17]*

## ***VI. Compressor Maps***

Compressor Maps for the NPSS model are the engine baseline mixed flow compressor maps. Attention was paid on maintaining a stall margin of at least 10% throughout the entire flight profile. Compressor maps are vital when calculating off design performance, as they determine the compressors efficiency and pressure ratio.

## ***VII. Final Compressor analysis***

After running both the fan and compressor analysis, a 2-stage transonic fan and 11-stage transonic high-pressure compressor with pressure ratios of 2.57 and 23.5, respectively are designed. Both compressors maintain a constant tip radius to prevent vibrational damage to the rotor blades. The HPC features 4 variable stators in the front 4 stages and bleed valves throughout to aid in startup, prevent stall at low RPM and allow for bleed air for customer use [13].

Figure 17 shows the general outline of both the Fan and HPC. Additionally, a basic outline of the swan neck duct is illustrated as well. The final fan stator blade is separated by 5

inches from the splitter and the initial swan neck length is estimated to be 10 inches. Both these values are estimated from the baseline 2D flow path created using WATE.

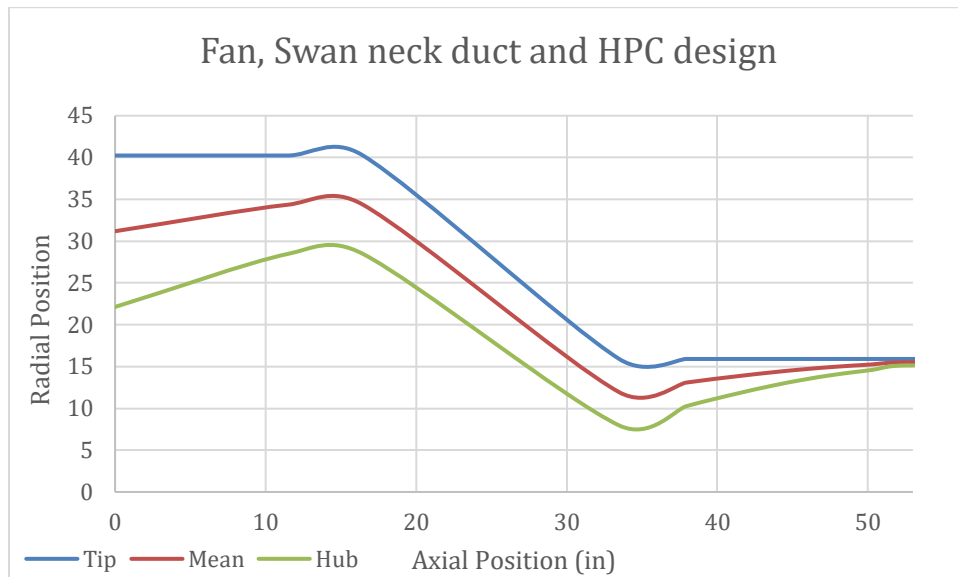


Figure 17: Fan, Swan neck duct and HPC Sizing

The use of Carbon fiber greatly reduces the impact of high aspect ratio design choice. This leads to an 8% increase in weight to the fan. However, the use of CMCs in the compressor led to an almost 40% decrease in weight of the HPC.

## 10. Burner

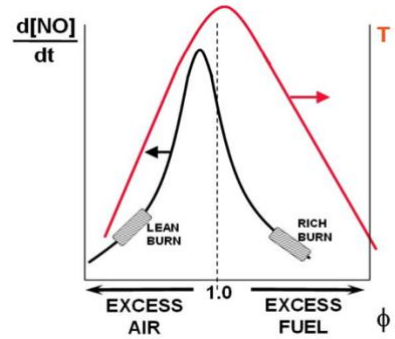
### I. Design

The candidate engine implements a Rich-Burn, Quick-Mix, Lean-Burn (RQL) combustor. The RQL begins with a rich burn at a 1.8 mixture ratio in the primary area. This rich burn enhances the stability and efficiency of the combustion reaction and minimizes NO<sub>x</sub> production due to low temperatures [20]. The rich burn leaves a high concentration of partially oxidized

Mass flow (lb)	177.975
Corrected mass flow (lbm)	14.62
Inlet Pt (psi)	352.641
Inlet Tt (R°)	2015.29
Inlet FAR	0.00
Inlet MN	0.1951
Inlet Area (in <sup>2</sup> )	132.7
Pressure change	0.975

Table 20: Burner Inlet Flow Conditions

products. Thus, more air is mixed in to complete the combustion reaction. As shown to the right, most of the NO<sub>x</sub> emissions are produced when the fuel mixing ratio is close to .8-.9. Thus, the area between the rich burn and lean burn zones, the quick mix zone, is where most of the NO<sub>x</sub> emissions are formed. The design's RQL combustor is modular in design (connected by flanges) and consists of five components: the headstock, the quick mix zone, the lean zone, and the exhaust section. This is done to allow variable component geometry. A team has already constructed such an RQL combustor in the past [19]; however, this model is designed for production.



Equation 16: Production of NO<sub>x</sub> vs Fuel mixing ratio

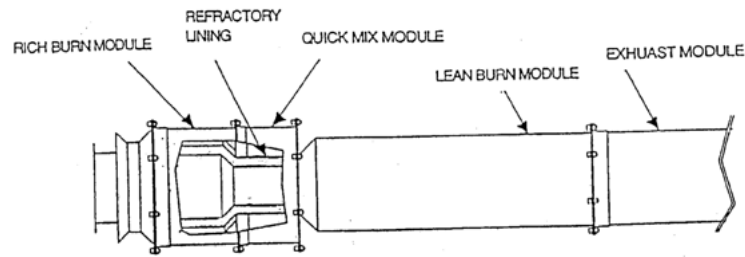


Figure 18: RQL Design [19]

The downside of a RQL combustor is that it prevents traditional film cooling of the combustor due to the formation of lean burn zones in the rich zone. This is fixed via the use of a CMC lined combustor. In recent years, according to Peterson, Sowa, and Samuelsen, a model RQL combustor is created using Hastelloy X (a nickel-based super alloy) combined with a high temperature refractory that lined the inner walls to survive temperatures more than 2100 K [19]. It is theorized that, by 2025, there will be sufficient advances in the field of CMCs to allow the construction of combustion chambers capable of withstanding such high temperatures. Additionally, the method of transpiration cooling will reduce the lean areas in the rich burn zone while still effectively cooling and maintaining combustor lifespan.

The RQL combustor holds a major advantage over the Lean, Premixed, Pre-vaporized (LPP) combustor because of its high stability [13]. While NO<sub>x</sub> emissions are slightly higher with the RQL combustor, this is minimized with a better quick mix jet air zone, which in turn limits the time at a mixing ratio of 1. Emissions are also minimized by decreasing the amount of swirl in the rich zone. Finally, according to NASA, the combustion efficiency will exceed 99% if the combustor inlet air temperature is greater than 367 K or 660 R. With an inlet combustor air temperature of almost 3 times that, it is assumed that the combustion efficiency for the RQL burner is the same as that which was modeled in the baseline engine.

## II. NO<sub>x</sub> Emissions

Emissions for commercial aircraft are important parameters to monitor. For supersonic aircraft both LTO cycle emissions and supersonic cruise emissions are considered. Emissions for both stages are calculated using the formula below found in the NPSS code [5].

$$EINO_x = .0041941 * (Pt3/439)^{.37} * exp((Tt3 - 1471)/345) * Tt4$$

*Equation 17: NO<sub>x</sub> Emissions Equation*

Although the design has a supersonic cruise EINO<sub>x</sub> value roughly 2.64 times that of the baseline engine, the fuel-to-air ratio is 9.2% less than the baseline, and (correspondingly) the required fuel flow-rate is 4.6% less than the baseline [2]. Thus, emissions are reduced simply by creating a more efficient engine.

The LTO cycle emissions data is shown to the right. The candidate engine meets the requirement of 181.1 g/kN by a significant margin.

<b>Segment</b>	<b>Power</b>	<b>Time</b>	<b>NO<sub>x</sub></b>
Takeoff	100	1.2	41.36
Climb out	65	2	28.35
Descent	15	1.2	4.52
Approach	34	2.3	15.31
Taxi/Idle	5.8	26	47.37
<b>Total</b>			<b>136.91</b>

*Table 21: LTO Cycle Emissions Data*

## 11. Turbines

### I. Turbine Design Strategy

As is the case for the compressor, much of the design is based on a few design choices and inlet conditions. In the case of the HPT and LPT, the shaft speed is set by the HPC and fan respectively. Again, the mean line is chosen as point of analysis. Adiabatic flow across the nozzles and constant axial velocity is assumed to simplify calculations. To begin analysis, the first nozzle in the turbine is choked. An assumed supersonic absolute Mach number and  $\alpha_2$  determine axial velocity. The figure below demonstrates the sign convention and naming scheme of the velocity triangle variables.

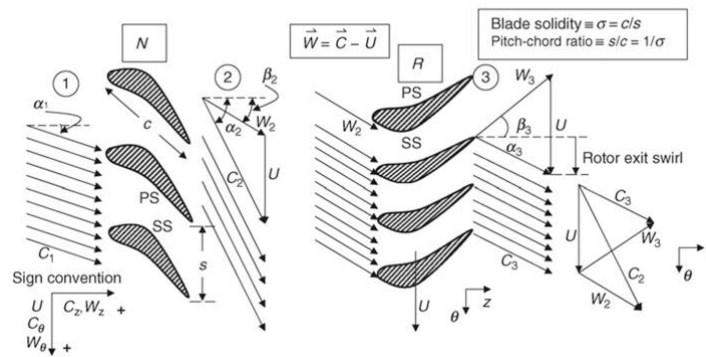


Figure 19: Turbine Velocity Triangle Notation [13]

The angles and velocities between the nozzle and rotor of the stage are determined using geometric relationships and the design choices of the initial mean line radius. Following this, rotor exit angles and velocities are calculated by choosing a relative exit Mach number ( $M_{3abs}$ ). Equation 16 define  $W_{\theta 3}$  which aids in establishing other exit velocities and angles.

$$W_{\theta 3} = -\sqrt{\frac{M_{3r}^2 [a_2^2 + (\gamma_t - 1)W_{\theta 2}^2/2] - C_{z2}^2}{1 + (\gamma_t - 1)M_{3r}^2/2}}$$

*Equation 18: Wtheta3 Calculation for Turbine*

Total and static pressures and temperatures throughout the stage are calculated using the Euler turbine equation, adiabatic relationships, and the isentropic relationships.

Close examination of the stage power output is required to correctly match the shaft power needed.

$$w_t = U_m (C_{\theta 2} - C_{\theta 3})$$

*Equation 19: Specific Work of Stage*

$$\dot{Q}_{stage} = \dot{m}_{stage} (w_t)_{stage}$$

*Equation 20: Power produced by Stage*

Finally, the annulus is sized. For both the LPT and HPT a constant tip radius is selected. Constant tip radii provide weight savings, better mixer integration and reduce blade stresses. Annulus area is derived using Equation 21.

$$\dot{m}_1 = \sqrt{\frac{\gamma_t}{R_t}} \frac{P_{t1}}{\sqrt{T_{t1}}} A_1 M_{z1} \left(1 + \left(\frac{\gamma_t - 1}{2}\right) M_{z1}^2\right)^{-\frac{\gamma_t + 1}{2(\gamma_t - 1)}}$$

*Equation 21: Annulus Area*

Blade height is then determined using the initial mean line radius. mean line and hub radii are then adjusted accordingly.

$$r_{t1} - r_{h1} = \frac{A_1}{2\pi r_m}$$

*Equation 22: Blade Height*



## I. High Pressure Turbine

As mentioned above, the High-Pressure Turbine shaft speed is controlled by the HPC. Inlet conditions are set by the exit of the burner; however, the flow must be accelerated to an appropriate speed prior to entering the first nozzle of the HPT.

Mass flow (lb)	182.224
Corrected mass flow (lbm)	19.80
Inlet Pt (psi)	343.790
Inlet Tt (R°)	3350.00
Inlet FAR	0.0239
Inlet MN	0.0995
Inlet Area (in <sup>2</sup> )	352.4
Pressure rise across HPT	0.1495

Table 22: HPT Inlet Flow conditions

Basic design values consisting of nozzle exit absolute Mach number and absolute exit angle are chosen. Additionally, the mean line radius is set at the exit compressor mean line and varied until Turbine power conditions are met. Exit rotor relative Mach number and absolute exit nozzle angle are set in accordance to the standards set by Farokhi [13].

Alpha2	70
Absolute Mach 2	1.2
Relative Mach 3	0.9
Alpha 4	61.5

Table 23: HPT Initial Design Choices

Due to the rotors motion, it only experiences a relative total temperature of 2950 Rankine. Thus, only the first HPT nozzle and first HPT rotor require cooling. Velocity triangles at the mean line as well as the important turbine parameters are included below.

HPT Stage	1		2	
	Nozzle	Rotor	Nozzle	Rotor
Zweifel Coefficient	1.00		1.00	
AN <sup>2</sup>	3.30E+10		6.51E+10	
Stage Pressure Ratio	0.35		0.47	
Work Coefficient	-1.85		-1.29	
Flow Coefficient	0.62		0.66	
Hub-to-Tip Ratio	0.86	0.86	0.73	0.71
Mean radius	14.93	14.93	13.89	13.71
Number of Blades	86	91	37	42
Aspect Ratio	2.10	2.00	2.2	2.00
Taper Ratio	0.7		0.7	
Tip Speed	1776.48		1776.48	
Stagger Angle	31.95	-10.72	23.80	-17.48
Blade chord	1.03	1.09	2.08	2.31
Degree of Reaction	0.23		0.42	
MN Absolute	0.38	1.20	0.45	0.92
MN Relative	0.38	0.62	0.93	0.46
Turbine Rotor Inlet Temperature	2950		2319	

Table 24: HPT Design Values at Mean line

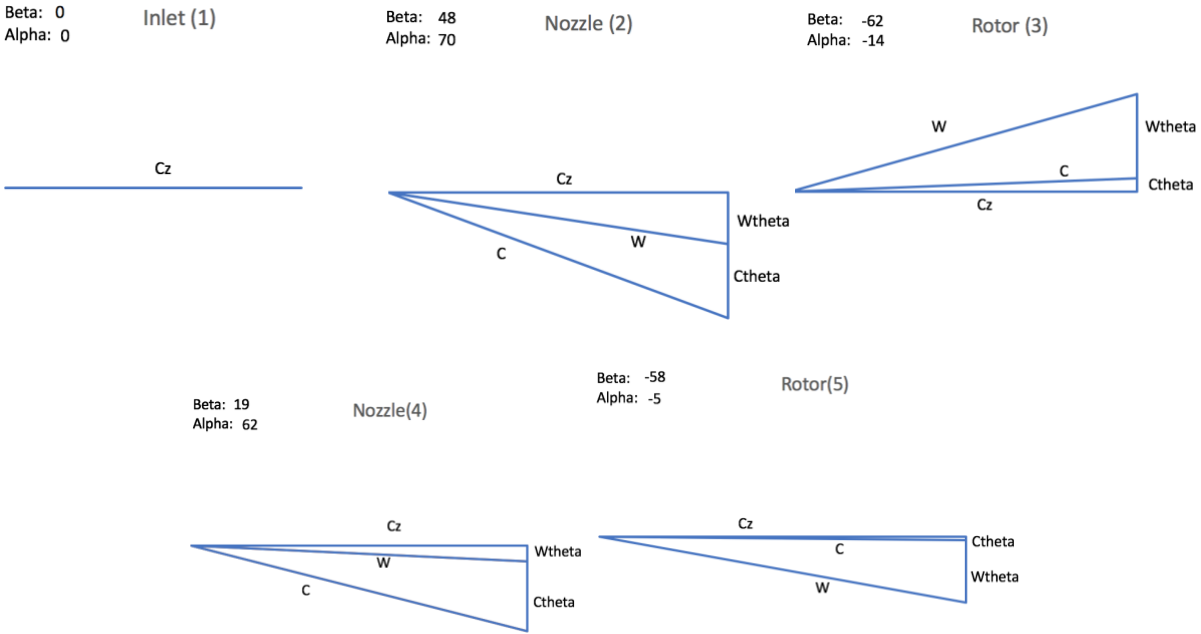


Figure 20: Velocity Triangles at Mean line for HPT

## II. Low Pressure Turbine

The LPT design process closely matches that of the HPC. The fan shaft speed is relatively low at 4949 RPM compared to the HP shaft. To compensate a higher mean line radius is needed. Iterations begin at the exit mean line of the HPT and are increased until goals were met. The fan power required is achieved in two stages by the virtue of a higher mean line radius.

The assumption of zero inlet swirl is maintained for simplicity despite the existence of a 5-degree HPT exit swirl. Further iterations of absolute exit nozzle angles allow an exit angle of 0.15 degrees. Table 21 lists the initial design white Table 22 contains the major LPT parameters.

Mass flow (lb)	187.728
Corrected mass flow (lbm)	112.45
Inlet Pt (psi)	51.422
Inlet Tt (R°)	2278.53
Inlet FAR	0.0232
Inlet MN	0.3946
Inlet Area (in <sup>2</sup> )	544.0
Pressure rise across LPT	0.2871

Table 26: LPT Inlet Flow Conditions

Alpha2	66
Absolute Mach 2	1.2
Relative Mach 3	0.9
Alpha 4	57.5

Table 25: Initial Design Choices LPT

LPT Stage	1		2	
	Nozzle	Rotor	Nozzle	Rotor
Zweifel Coefficient	1.00			
AN <sup>2</sup>	2.37E+10		3.85E+10	
Stage Pressure Ratio	0.42		0.61	
Work Coefficient	-2.69		-1.68	
Flow Coefficient	0.98		1.07	
Hub-to-Tip Ratio	0.76	0.76	0.61	0.57
Mean radius	23.62	23.59	21.62	21.07
Number of Blades	48	46	26	23
Aspect Ratio	2.10	2.00	2.20	2.00
Taper Ratio	0.70		0.70	
Tip Speed	1159.46		1159.46	
Stagger Angle	23.63	-4.17	21.46	-4.24
Blade chord	3.08	3.25	5.20	5.78
Degree of Reaction	0.14		0.16	
MN Absolute	0.45	1.20	0.57	0.95
MN Relative	0.45	0.77	0.93	0.61
Turbine Rotor Inlet Temperature	2082		1713	

Table 27: LPT Design Values at Mean line

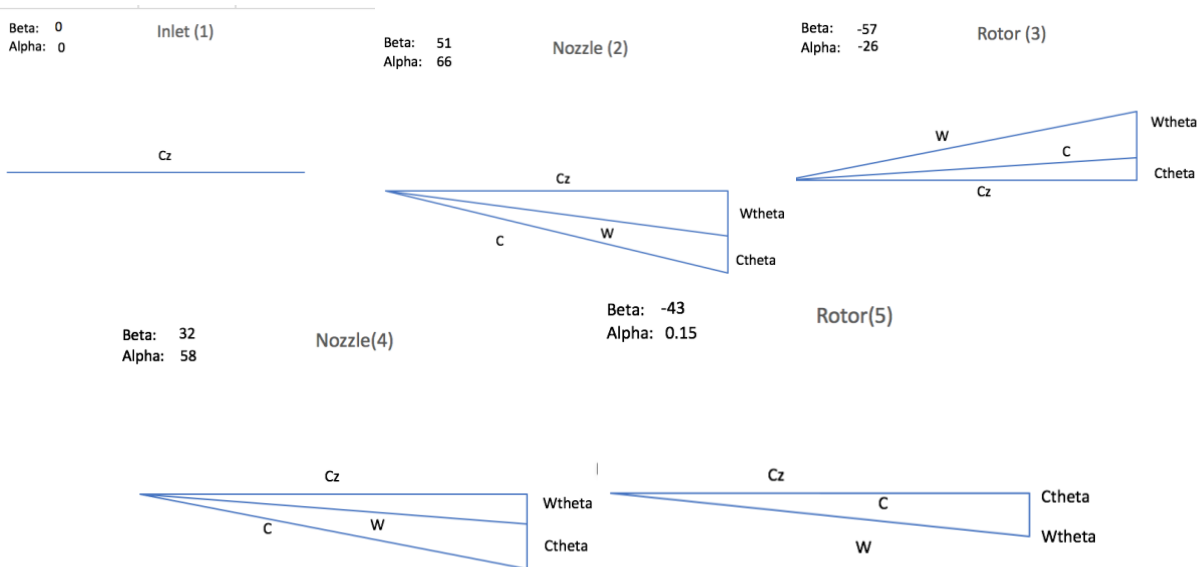


Figure 21: Velocity Triangles at Mean line for LPT

### III. Blade Stress and Material selection

Once again, turbine temperatures and centrifugal stresses are considered when calculating stresses. Temperature stress is ignored, as it reduces the centrifugal stresses felt by the blade due. Thus, if the blades can withstand the centrifugal stress, the temperature limits will not cause

failure. Using the methods described in the compressor section the blade stresses are calculated and the appropriate materials chosen. To check the blade stress conditions and confirm the validity of the turbine design,  $AN^2$  values are checked and compared to the limits below.

– **Typical Limits:**

- Cooled Blade  $< 5 \times 10^{10}$
- Advanced Technology  $< 6.5 \times 10^{10}$
- Uncooled Solid Blade  $< 10 \times 10^{10}$
- LPT  $< 7 \times 10^{10}$

*Figure 22:  $AN^2$  Typical Limits [24]*

The blade stress calculations and decisions are outlined below. CMCs are used throughout the turbine design to optimize for low weight while still maintaining a long lifecycle and more “on wing time”. Positive stress margins are maintained throughout.

	HPT Stage 1	HPT stage 3	LPT stage 1	LPT stage 1
Relative Tt (°R)	2950	2319	2082	1713
Specific strength required (ft <sup>2</sup> /s <sup>2</sup> )	49016082	96535142	35095229	57049586
Material Chosen	Ceramic Matrix Composites (CMC)	Ceramic Matrix Composites (CMC)	Ceramic Matrix Composites (CMC)	Ceramic Matrix Composites (CMC)

*Table 28: Blade Stress and Material Selection Turbine*

While a blisk design is optimal for both the LPT and HPT turbines, only the LPT features one. Due to the nature of the HPT, blades will more often need to be replaced and repeatedly manufacturing a brand new blisk is not economically viable.

#### ***IV. Final Turbine Design***

After running the HPT and LPT analysis a two stage HPT and a two stage LPT are designed. The LPT design reduces the number of stages by 50% compared to the baseline engine and the use of CMC in the turbines reduces engine weight by 17%.

The first HPT stage utilizes 3% bleed air from the compressor to cool the nozzle and rotor. Reading off the smith chart, each turbine stage maintains an efficiency of at least 88%.

The initial outline for the turbines and inter turbine duct is included in Figure 23. The length of the inter duct is again measured off the baseline WATE++ model.

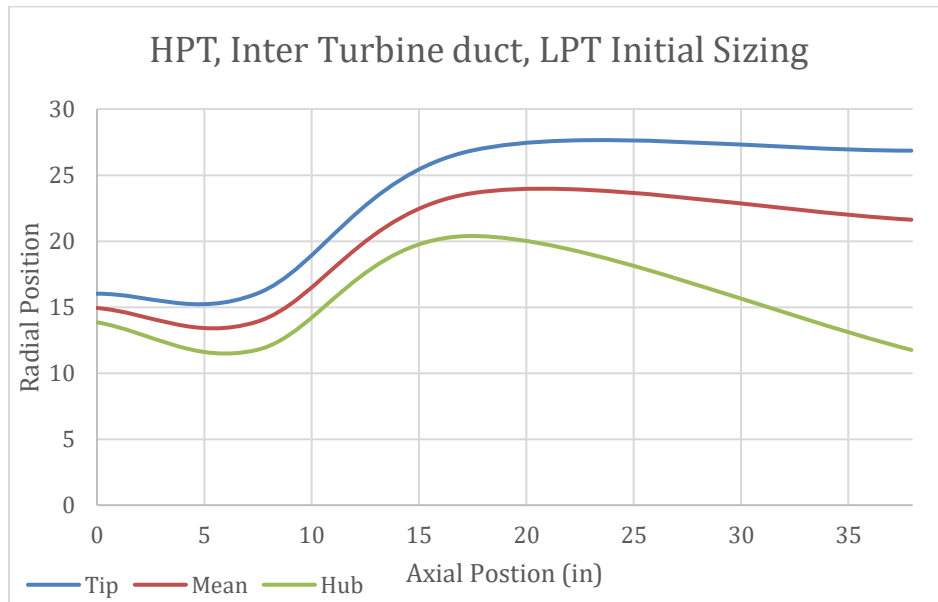


Figure 23: HPT, Inter Turbine duct, LPT Initial Sizing

## 12. Variable Cycle Implementation

Two variable sections are required to achieve the proposed VCE architecture. A variable part in the splitter area is needed to change the amount of bypass air and a variable mixer or a VABI is needed to match the static pressures.

### I. Variable bypass Design

The change in mass flow at different design points, as well as weight and complexity concerns must be noted. A variable bleed system capable of bleeding air from the swan neck duct to the bypass duct using vents controlled by a fuel hydraulic system is proposed. This system is preferred over a heavy counterpart that changes the area of the splitter bypass duct entrance for its simplicity and weight savings. One main set and a smaller set of these variable

bleed ducts can be opened to achieve the optimum BPR for a specific flight condition. However, the swan neck pressure must be higher than the BP duct pressure to properly function.

The mass flow and vent area must be calculated to design the bleed system from the swan neck duct to the bypass duct. Using the Poiseuille equation, shown below, the swan neck bleed vents for SLS are designed.

$$\Delta P = \frac{8\mu LQ}{\pi R^4}$$

*Equation 23: Poiseuille equation*

Delta P is the pressure differential, R is the pipe radius,  $\mu$  is the dynamic viscosity, L is the length of the pipe and Q is the volumetric flow rate. After rearranging, and converting Q into W, mass flow, using air density, the radius can be calculated. NPSS provides the Delta P.  $\mu$  and density are approximated using the outlet splitter conditions. L is roughly 10 inches according to the WATE 2D flowpath. At design point, an area of 17.64 in<sup>2</sup> is needed to achieve the optimal BPR. Estimating the vent will be at the end of the swan neck duct, the vent will only need to be about .2 inches wide. More testing using CFD is required to optimize vent sizing.

## **II. VABI Mixer**

A mixer combines two flows while maintaining momentum and matching static pressures of the two flows. In a VCE, static pressures of the two flows will change as BPR changes. To solve this issue, a Variable Area Bypass Injector (VABI) is installed. The VABI changes the rear area of the bypass duct either by speeding up or slowing down the bypass duct airflow. This in turn allows a matched static pressure. Below is a simple drawing of the VABI YJ-594 has installed.

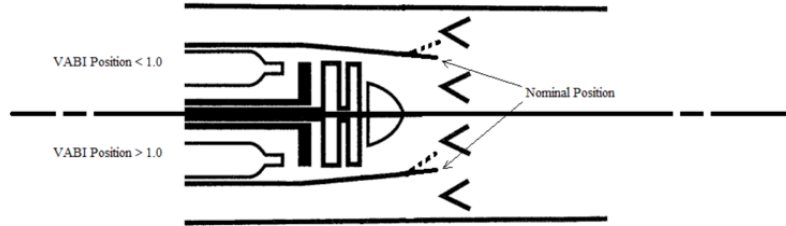


Table 29: VABI Positioning Diagram[9]

The changing area element acts as a variable nozzle. A ring precedes the mixer with a series of plates attached. As the flight regime changes, the ring moves forward or backward using hydraulics. When pushed toward the engine nozzle, the ring causes the plates to point inward and increases bypass duct area. When the ring is pushed toward the engine fan, the plates point outward and the bypass duct area becomes smaller. The movement of the ring is controlled by an onboard computer. Rather than carry heavy hydraulic fluid onboard, fuel is used in its stead. According to the GasTurb manual, the VABI position is restricted between .5 and 1.5, and the bypass duct may vary from 0.5-1.5x its size [7]. This is not an issue as minimum TSFC is reached before this sizing becomes restrictive.

### ***III. Efficiency***

Typically, a good forced mixer matches the total pressures of the flows as well as the Mach numbers. With a VABI, the Mach numbers are drastically different and static pressure drops must occur for correct mixing. When the VABI is active, the total pressure ratio does not rise above 1.05. Thus, mixing losses are modeled in the same way as the baseline engine.

## **13. Nozzle**

### ***I. Design of Nozzle***

It is valuable to compare the thrust gains nozzles when choosing a design. Two options are explored for the candidate engine—the simple, light converging nozzle, and the heavier but

more efficient converging diverging nozzle. Using information from the baseline model, the design point nozzle PR and gamma at nozzle inlet are calculated.

Figure 22 is used to estimate a 7% increase in gross net thrust via the use of a converging diverging nozzle. This thrust gain at design point makes the installation of a converging diverging nozzle worth the added weight.

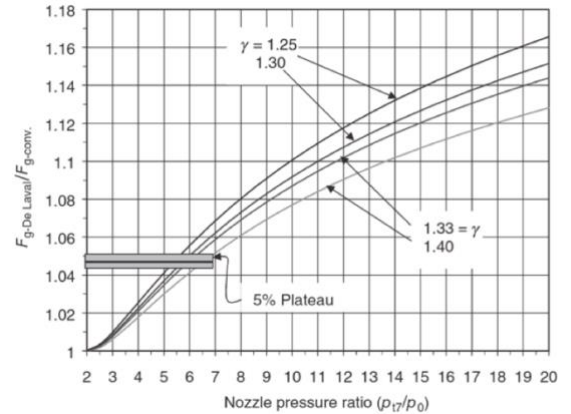


Figure 22: Performance of a CD nozzle vs. a Convergent nozzle

There is however, no compelling reason to include a fully variable nozzle. The weight penalties, the inclusion of the VABI and the lack of afterburner all factored into the decision to not install this type of C-D nozzle. A passive diverging section is utilized instead. The throat area remains constant while the internal pressure of the nozzle provides enough force to position the nozzle exit area to its optimum flight point [27].

## II. Noise

The diverterless inlet's inherent ability to divert boundary layers around the intake, noise is already reduced in comparison to alternative approaches (particularly propeller based counterparts). This passive in-built noise reduction is supplemented with Boeing's retractable noise suppression system [21] consisting of acoustically treated foil members positioned along the inlet walls. These segments are extended into operation during take-off and split inlet flow, reducing sound pressure levels and ultimately ground noise. The foils are retracted and stored in auxiliary intake passageways during other stages of flight.

Engine exhaust noise is tackled with a similarly passive methodology involving acoustic lining designed specifically to attenuate sounds operating at the compressor blades' primary



frequency. This lining is constructed from ceramic matrix composite (which is moderately lighter than traditional aluminum) and forms a honeycomb base structure with perforated glass lining. This system, known as a Helmholtz resonator, [22] contains fluid oscillates at the blade frequency and facilitates noise damping. The dominant frequency is calculated using:

$$f = \frac{B * n}{60}$$

*Equation 24: Dominant Frequency*

Where **B** is the compressor blade angular frequency (in RPM) and **n** is the number of blades. Following the formula yields a principal blade frequency range of 1650-8743 Hz caused primarily by the low power shaft—well within the limits of human hearing. Tuning the acoustic lining to a frequency between these values reduces noise significantly and only adds 3.35 lbs. to overall engine weight. The slight increase in mass and surface drag is acceptable given this mechanism's noise reduction efficacy.

Exhaust noise reduction is analyzed in conjunction with weight minimization and performance losses. A mixer injector nozzle is heavy and incapable of providing sufficient benefits. A set of variable wedges are instead installed onto the diverging element of the engine. These wedges/ramps rise a few degrees during takeoff and landing, and act like a corrugated internal mixer [25]. The subsequent increase in strength of high frequency sounds (notably stemming from the high-power compressor shaft) is mitigated using this noise suppressing nozzle to maximize to cause absorption into the atmosphere [23]. While this solution does not directly influence exit jet velocity, the mixing further downstream of the engine acts like an engine with a low exit jet velocity.

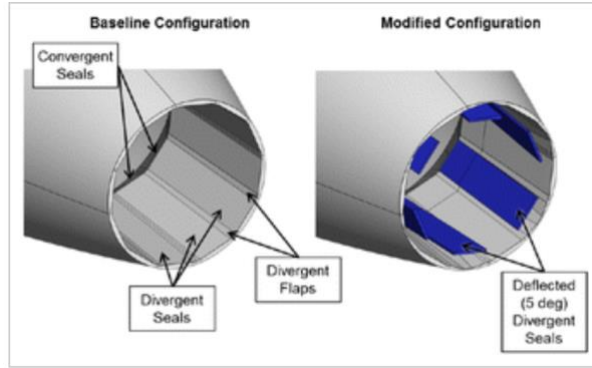


Figure 24: Proposed Noise Suppressor [25]

These ramps function as the chevron nozzles displayed in new high bypass engines without adversely impacting thrust and providing increased noise reduction.

Studies reaffirm that thrust remains unaltered. Due to its passive control, the nozzle expands to compensate for any area reduction caused by ramp deployment. Due to the variable nature of the ramps and their position in the nozzle interior, cruise performance is also uninhibited and no drag penalties are imposed.

### III. Final Nozzle Design

The final nozzle design is an axisymmetric, converging diverging nozzle with passive control features. A series of variable ramps deploy during takeoff and landing, increasing mixing at nozzle exit. Area scheduling and associated gross thrust coefficient and drags are displayed in Table 25. Due to the similarity in sizes

Mass flow (lb)	590.829
Corrected mass flow (lbm)	877.27
Inlet Pt (psi)	14.508
Inlet Tt (R°)	1114.50
Inlet FAR	0.0072
Inlet MN	0.2009
Inlet Area (in <sup>2</sup> )	7626.7
Pressure Gain	9.727

Table 30: Nozzle Inlet Flow Conditions

compared to the baseline model, the RFP approach is used to model these parameters.

Segment	Throat Area (in <sup>2</sup> )	Exit Area (in <sup>2</sup> )	Gross thrust coefficient	Nozzle Drag (lbf)
Cruise	2571.28	4912.4	0.9603	588
Transonic Pitch	2571.28	3461.2	0.9716	332
Takeoff	2571.28	2616.4	0.9330	0

Table 31: Nozzle Performance

Due to the design of the nozzle, major weight savings are expected compared to the baseline model. These weight savings are magnified by selecting ceramic matrix during the manufacturing process.

#### 14. Conclusion

The candidate engine outlined above has provided significant weight and fuel savings. The new engine saves a combined weight of 6392 lbs. If this reduction is utilized solely to maximize range, flight distance can be improved by 480 nm for a new max range of 4500 nm. This 480-nm increase is approximately the distance from Washington D.C. to Atlanta, Georgia.

Parameter	Required Value	Design Value	Margin Relative to Requirement
Takeoff Thrust (lbf)	64625	64625	0.00%
Max Thrust at Transonic Pinch Point (lbf)	14278	16916	18.46%
TSFC at Transonic Pinch Point (lbm/hr/lbf)	0.950	0.8825	-7.64%
Max Thrust at Supersonic Cruise (lbf)	14685	14928	1.65%
TSFC at Supersonic Cruise (lbm/hr/lbf)	1.091	1.0324	-5.37%
Fan Diameter (in)	87.5	80.5	-8.00%
Bare Engine Weight (excl. inlet) (lbm)	13000	11870	-8.69%
Takeoff Exhaust Jet Velocity (ft/sec)	1375	1556	13.16%
LTO NOx (g/kN)	179.92	134.97	-25.02%
Supersonic Cruise NOx (g/kg)	5	42.68	853.6%

Table 32: Performance Requirements Matrix

As shown in Table 26, the candidate engine meets all required values by the RFP except for the supersonic NOx emissions and the exit jet velocity. However, both parameters have proposed solutions that minimize their impact toward the environment. The exit jet velocity design value is possibly overstated and its noise impact is greatly reduced due to the innovations presented above. While the supersonic cruise NOx emission is quite high, the hope new innovations in RQL combustor technology will lower these values significantly in the coming years.

More information regarding the design point flow station parameters and other important NPSS parameters as well as hand calculations for turbomachinery velocity triangles are in the Appendices.

In conclusion, the candidate engine will provide significant fuel and weight savings leading to a 12% increase in range while subject to technological and cost constraints present in 2025.

## References

1. Sóbester, András. "Wing Sizing via Constraint Analysis." Aircraft Geometry Codes, Wordpress, 31 Oct. 2016, [aircraftgeometrycodes.wordpress.com/2016/10/31/wing-sizing-via-constraint-analysis/](http://aircraftgeometrycodes.wordpress.com/2016/10/31/wing-sizing-via-constraint-analysis/).
2. American Institute of Aeronautics and Astronautics, "Candidate Engines for a Next Generation Supersonic Transport," 2017-2018 AIAA Undergraduate Team Engine Design Competition
3. Welge, Harry R. "N+2 Supersonic Concept Development and Systems Integration ." NASA Langley Research Center, 1 Aug. 2010, [ntrs.nasa.gov/search.jsp?R=20100030607](http://ntrs.nasa.gov/search.jsp?R=20100030607).
4. Roskam, Jan. Airplane Design: Preliminary Sizing of Airplanes. DAR Corporation, 1997
5. Lytle, John. "The Numerical Propulsion System Simulation: An Overview." June 2000, [ntrs.nasa.gov/archive/nasa/casi.ntrs.nasa.gov/20000063377.pdf](http://ntrs.nasa.gov/archive/nasa/casi.ntrs.nasa.gov/20000063377.pdf).
6. Tong, Michael. "An Object-Oriented Computer Code for Aircraft Engine Weight Estimation." Dec. 2009, [ntrs.nasa.gov/archive/nasa/casi.ntrs.nasa.gov/20100000016.pdf](http://ntrs.nasa.gov/archive/nasa/casi.ntrs.nasa.gov/20100000016.pdf).
7. Joachim, Joachim. "GasTurb13 Manual." 2018, [www.gasturb.de/Gtb13Manual/GasTurb13.pdf](http://www.gasturb.de/Gtb13Manual/GasTurb13.pdf).
8. "GE Adaptive Cycle Engine." GE Aviation, 2017, [www.geaviation.com/military/engines/ge-adaptive-cycle-engine](http://www.geaviation.com/military/engines/ge-adaptive-cycle-engine).
9. Ford, Sean. "THERMODYNAMIC CYCLE DESIGN AND OPTIMIZATOIN METHOD FOR AICRAFT ENGINES." Georgia Institute of Technology, 2014.
10. Moxon, Julian (1989). ATF rivals ready for engine contest. Flight International. 15-21 Nov 1989
11. Tedeschi, Diane. "How Things Work: Supersonic Inlets." Air & Space Magazine, Air & Space Magazine, 1 Nov. 2002, [www.airspacemag.com/military-aviation/how-things-work-supersonic-inlets-35428453/](http://www.airspacemag.com/military-aviation/how-things-work-supersonic-inlets-35428453/).
12. Serflek, Szabolcs. "Air Inlets." F-15E Strike Eagle.com - Pratt & Whitney F100-PW-220/229 Engine, [www.f-15e.info/joomla/technology/engines/100-air-inlets](http://www.f-15e.info/joomla/technology/engines/100-air-inlets).
13. Farokhi, Saeed. Aircraft Propulsion. Wiley, 2014.
14. Dixon, S. L. Fluid Mechanics and Thermodynamics of Turbomachinery. Butterworth-Heinemann, 1998.
15. "Why Composite Fan Blades Will Propel Future Jet Engines." GE Reports, 15 Sept. 2017, [www.ge.com/reports/the-art-of-engineering-the-worlds-largest-jet-engine-shows-off-composite-curves/](http://www.ge.com/reports/the-art-of-engineering-the-worlds-largest-jet-engine-shows-off-composite-curves/).
16. M. T. Tong, I. Halliwell, L. J. Ghosn, "A Computer Code for Gas Turbine Engine Weight and Disk Life Estimation," [<https://ntrs.nasa.gov/archive/nasa/casi.ntrs.nasa.gov/20020072843.pdf>], ASME Turbo Expo, Amsterdam, The Netherlands, June 2002.
17. GroupeSafran. "LEAP Engine - Blisk." YouTube, YouTube, 19 Sept. 2013, [www.youtube.com/watch?v=SniYFvF0TSk](http://www.youtube.com/watch?v=SniYFvF0TSk).
18. "GE9X Commercial Aircraft Engine." GE Aviation, [www.geaviation.com/commercial/engines/ge9x-commercial-aircraft-engine](http://www.geaviation.com/commercial/engines/ge9x-commercial-aircraft-engine).
19. C. O. Peterson, W. A. Sowa, and G. S. Samuelsen, "Performance of a Model Rich Burn-Quick Mix-Lean Burn Combustor at Elevated Temperature and Pressure," [<https://ntrs.nasa.gov/archive/nasa/casi.ntrs.nasa.gov/20030013952.pdf>], NASA, University of California, Irvine, CA, December 2002.

20. Samuelsen, Scott, "Rich Burn, Quick-Mix, Lean Burn (RQL) Combustor," [https://netl.doe.gov/File%20Library/Research/Coal/energy%20systems/turbines/handbook/3-2-1-3.pdf], Department of Energy, University of California, Irvine, CA.
21. Farokhi, S., "A Trade-Off Study of Rotor Tip Clearance Flow in a Turbine/Exhaust Diffuser System," Volume 9: 23rd International Conference on Design Theory and Methodology; 16th Design for Manufacturing and the Life Cycle Conference | IDETC/CIE2011 | Proceedings | ASME  
DCAvailable:http://proceedings.asmedigitalcollection.asme.org/proceeding.aspx?articleid=2213567.
22. Langenbrunner, N., Weaver, M., Dunn, M. G., Padova, C., and Barton, J., "Dynamic Response of a Metal and a CMC Turbine Blade During a Controlled Rub Event Using a Segmented Shroud," Volume 7B: Structures and Dynamics, 2014.
23. "Noise Control (Supression)," What is Cellulose - Purdue NanoForestryAvailable:https://engineering.purdue.edu/~propulsi/propulsion/jets/basics/noise.html.
24. Treuren, Kenneth. "EGR 4347 PowerPoint Slides." Powerpoint, web.ecs.baylor.edu/faculty/vantreuren/EGR4347/egr\_4347\_powerpoint.htm
25. Pilon, Anthony R. et al., "Design and Analysis of a Supersonic Jet Noise Reduction Concept," [https://arc.aiaa.org/doi/pdf/10.2514/1.C033977], AIAA Journal of Aircraft, October 2017.
26. Pike, John. "Military." Globalsecurity, www.globalsecurity.org/military/systems/aircraft/dsi.htm.
27. Gamble, Eric. "Nozzle Selection and Design Criteria." Apollo 13 Guidance, Navigation, and Control Challenges | AIAA SPACE 2009 Conference & Exposition, AIAA, July 2004, arc.aiaa.org/doi/10.2514/6.2004-3923.

Summary Output Data														
MN	alt	dTamb	W	Fg	Fn	TSFC	BPR	VTAS	OPR	T4	T41	humRel		
1.600	52500.0	0.00	606.92	44191.3	15851.0	0.9650	2.17501	1549.57	59.791	3350.0	3313.6	0.000		
INSTALLED PERFORMANCE														
Wengine	Wbypass	Wbleed	Fram	FgIn	FnIn	TSFCin	eRam	Dinlet	Dnozz	Acapt	A0AC	Fan Diam		
588.43	0.00	18.48	28340.3	43148.5	14808.2	1.0329	0.9535	453	589	6481	0.8173	80		
FLOW STATION DATA														
		W	Pt	Tt	FAR	ht	Wc	Ps	Ts	Aphy	MN	Rt	gamt	
FS0	InEngStart.Fl_0	606.917	6.342	590.07	0.0000	141.09	1500.06	1.492	389.97	5463.2	1.6000	0.0686	1.39920	
FS1	Inlet.Fl_0	588.434	6.047	590.07	0.0000	141.09	1525.33	5.081	561.48	5915.2	0.5049	0.0686	1.39920	
FS17	Inlet.BypassOut	0.000	14.696	518.67	0.0000	0.00	0.00	0.000	0.00	0.00	0.0000	0.0686	1.40052	
IB0	Inlet.BleedOut	18.483	6.047	590.07	0.0000	141.09	47.91	0.000	0.00	0.00	0.0000	0.0686	1.39920	
FS2	IGVDuct.Fl_0	588.434	5.986	590.07	0.0000	141.09	1540.74	5.391	572.69	7293.8	0.3898	0.0686	1.39920	
FS21	Fan.Fl_0	588.434	15.385	793.27	0.0000	190.18	695.11	13.823	769.67	3261.5	0.3950	0.0686	1.39227	
FS13	Split.Fl_02	403.101	15.385	793.27	0.0000	190.18	476.18	13.782	769.02	2208.7	0.4006	0.0686	1.39227	
FS23	Split.Fl_01	185.333	15.385	793.27	0.0000	190.18	218.93	13.542	765.22	956.3	0.4318	0.0686	1.39227	
FS25	SwanNeckDuct.Fl_0	185.333	15.231	793.27	0.0000	190.18	221.14	13.759	770.84	1060.2	0.3848	0.0686	1.39227	
FS3	HPC.Fl_0	183.480	357.938	2015.29	0.0000	508.97	14.85	323.882	1966.12	71.9	0.3900	0.0686	1.32776	
FS31	CDPBld.Fl_0	177.975	357.938	2015.29	0.0000	508.97	14.40	331.529	1977.51	78.2	0.3410	0.0686	1.32776	
FS32	OGVduct.Fl_0	177.975	352.641	2015.29	0.0000	508.97	14.62	343.853	2002.79	132.7	0.1951	0.0686	1.32776	
FS4	BrnPri.Fl_0	182.224	343.790	3350.00	0.0239	924.96	19.80	341.616	3345.32	352.4	0.0995	0.0685	1.28319	
FS45	HPT.Fl_0	187.728	51.422	2278.53	0.0232	599.24	112.45	46.505	2225.77	544.0	0.3946	0.0685	1.30351	
FS48	ITTduct.Fl_0	187.728	51.422	2278.53	0.0232	599.24	112.45	46.505	2225.77	544.0	0.3946	0.0685	1.30351	
FS5	LPT.Fl_0	187.728	14.764	1744.52	0.0232	445.33	342.71	13.315	1701.09	1638.0	0.3972	0.0685	1.32242	
FS56	TEGVduct.Fl_0	187.728	14.616	1744.52	0.0232	445.33	346.17	14.011	1726.62	2459.3	0.2534	0.0685	1.32242	
FS14	FanBld.Fl_0	403.101	15.385	793.27	0.0000	190.18	476.18	13.782	769.02	2208.7	0.4006	0.0686	1.39227	
FS16	BPduct.Fl_0	403.101	14.616	793.27	0.0000	190.18	501.24	14.011	783.86	3554.4	0.2473	0.0686	1.39227	
FS6	Mix.Fl_0	590.829	14.581	1114.50	0.0072	271.25	872.88	13.939	1101.04	6013.7	0.2574	0.0686	1.36848	
FS7	Tailpipe.Fl_0	590.829	14.508	1114.50	0.0072	271.25	877.27	14.115	1106.26	7626.7	0.2009	0.0686	1.36848	
FS9	NozPri.Fl_0	590.829	14.508	1114.50	0.0072	271.25	877.27	1.492	592.14	4920.2	2.1355	0.0686	1.36848	
TURBOMACHINERY PERFORMANCE DATA														
	Wc Wp	PR	eff	TR	effPoly	Nc Np	pwr	SMN	SMW					
Fan	1540.74	2.570	0.8923	1.3444	0.9055	99.4	-40867.9	22.53	24.91					
HPC	221.14	23.500	0.8534	2.5405	0.8993	85.7	-83174.7	21.00	24.92					
HPT	30.68	6.686	0.9098	1.4654	0.8897	1.8	83275.1							
LPT	174.26	3.483	0.9122	1.3061	0.8990	2.2	40880.2							
DUCTS														
	dPqP	MNin	Aphy											
IGVDuct	0.01000	0.5049	5915.25											
SwanNeckD>	0.01000	0.4318	956.35											
OGVduct	0.01480	0.3410	78.20											
ITTduct	0.00000	0.3946	543.98											
TEGVduct	0.01000	0.3972	1637.95											
BPduct	0.05000	0.4006	2208.71											
Tailpipe	0.00500	0.2574	6013.71											
BLEEDS - interstg														
	OB_Cust	HPC	OB_Cust	Wb Win	dhb dh	dPb dP	W	Tt	ht	Pt				
				0.0100	0.5000	0.2991	1.8533	1425.47	349.57	117.74				
BLEEDS - output														
	C_FS41	CDPBld	CDPBldA	Wb Win	hscale	Pscale	W	Tt	ht	Pt				
				0.0297	1.0000	1.0000	5.5044	2015.29	508.97	357.94				
				0.0000	1.0000	1.0000	0.0000	793.27	190.18	15.39				
SPLITTERS														
Split	BPR	dP/P1	dP/P2											
	2.17501	0.0000	0.0000											
SHAFTS														
	Nmech	trqIn	pwrIn	HPX										
ShH	105.960	4127693.8	83275.1	100.00										
ShL	106.020	2025159.1	40880.2	0.00										
BURNERS														
BrnPri	TtOut	eff	dPqP	Wfuel	FAR	EINOx								
	3350.00	0.9970	0.0251	4.24880	0.02387	42.6835765								
MIXERS														
Mix	PtRatio	MN1	MN2	partialMix										
	1.0000	0.253	0.247	0.9854										
NOZZLES														
NozPri	type	PR	Cfg	CdTh	Cv	Cang	CmixCorr	Cqua	Ath	MNth	Vactual	Fg	FgIdeal	Vid,full
	CON_DIV	9.727	0.9603	0.9630	1.0000	1.0000	0.9854	1.0000	2571.28	1.000	2543.2	44191.3	46701.3	2543.2

## APPENDIX A: NPSS OUTPUT FILE DESIGN POINT YF-594

Fan Stage 1

inlet conditions  
 MN = .39  
 T<sub>2</sub> = 561 °R  
 A = 7.293 ft  
 λ = 1.4  
 R = 1717 ft/lb-mole

design choices  
 Tip speed mach = 1.5  
 h/t = .55  
 de haller = 0.72

$C_2 = \sqrt{\lambda R T_2} \cdot MN = 451 \text{ ft/s}$

$r_{tip} = \sqrt{\frac{A}{(1-\lambda) \pi}} = 28.40 \text{ in}$       $r_{mean} = \frac{r_{tip} h/t + r_{hub}}{2} = 31.19 \text{ in}$

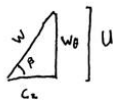
Tip Speed =  $MN \sqrt{\lambda R T_2} = 1737.95 \text{ ft/s} = U_{tip}$

shaft  $\omega = \frac{U_{tip}}{r_{tip}} = 5183 \text{ rad/s} = \omega$

shaft RPM =  $60 \frac{\omega}{2\pi} = 4948 \text{ RPM}$

Speed at mean =  $r_{mean} \omega = 1346.91 = U_{mean}$

nozzle



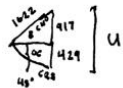
rotor  
 $W_2 = \sqrt{C_2^2 + W_0^2} = 1420.61 \text{ ft/s}$   
 $C_0 = C_2 = 1346.91 \text{ ft/s}$   
 $C_1 = C_2 = 451 \text{ ft/s}$   
 $\alpha_1 = 0^\circ$   
 $\beta_1 = \tan^{-1}(\frac{W_0}{C_2}) = 71.46^\circ$



blc repeating stage  
 $C_1 = C_2 = 451 \text{ ft/s}$   
 $\alpha_1 = \alpha_2 = 0^\circ$

stator

$W_2 = W_1$  de haller = .72  $1420.61 = 1022 \text{ ft/s}$   
 $\beta_2 = \cos^{-1}(\frac{C_2}{W_2}) = 63.8^\circ$   
 $W_0 = \sin \beta_2 \cdot W_2 = 917 \text{ ft/s}$   
 $C_0 = U - W_0 = 429 \text{ ft/s}$   
 $C_2 = \sqrt{C_0^2 + C_0^2} = 603 \text{ ft/s}$   
 $\alpha_2 = \tan^{-1}(\frac{C_0}{C_2}) = 43.54^\circ$



HPC stage 1

inlet conditions  
 T<sub>2</sub> = 770 °R  
 MN = .3846  
 A = 1060 ft  
 λ = 1.4  
 R = 1717

design  
 Tip speed 1.5  
 h/t .5  
 de haller .72  
 α = 5°

$C_2 = \sqrt{\lambda R T_2} \cdot MN = 522.38 \text{ ft/s}$

$r_{tip} = \sqrt{\frac{A}{(1-\lambda) \pi}} = 16.9 \text{ in}$       $r_{mean} = \frac{r_{tip} h/t + r_{hub}}{2} = 11.93 \text{ in}$

Tip Speed =  $MN \sqrt{\lambda R T_2} = 1764 \text{ ft/s} = U_{tip}$

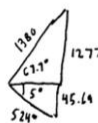
shaft  $\omega = \frac{U_{tip}}{r_{tip}} = 1331 \text{ rad/s}$

shaft RPM =  $60 \frac{\omega}{2\pi} = 12710 \text{ RPM}$

mean speed  
 $r_{mean} \omega = U_{mean} = 1723 \text{ ft/s}$

rotor

$C_2 = \frac{C_0}{\cos \alpha_2} = 524.82 \text{ ft/s}$   
 $C_0 = C_1 \tan \alpha_2 = 45.64 \text{ ft/s}$   
 $W_0 = U - C_0 = 1277.7 \text{ ft/s}$   
 $W_2 = \sqrt{W_0^2 + C_2^2} = 1380 \text{ ft/s}$   
 $\beta_2 = \tan^{-1}(\frac{W_0}{C_2}) = 67.76^\circ$



repeating stage  
 $C_1 = C_2 = 524.82$   
 $\alpha_1 = \alpha_2 = 5^\circ$

stator

$W_2 = W_1$  de haller = .943  $1723 \text{ ft/s}$   
 $\beta_2 = \cos^{-1}(\frac{C_2}{W_2}) = 58^\circ$   
 $W_0 = \sin \beta_2 \cdot W_2 = 845 \text{ ft/s}$   
 $C_0 = U - W_0 = 477 \text{ ft/s}$   
 $\alpha_2 = \tan^{-1}(\frac{C_0}{C_2}) = 47.5^\circ$   
 $C_1 = \sqrt{C_0^2 + C_0^2} = 707.96 \text{ ft/s}$



LPT Conditions

T<sub>2</sub> = 2278.53 °R  
 W = 4498 RPM  
 λ = 1.3  
 R = 1716

LPT stage 1

design choices  
 $r_{mean} = 23.62$   
 $\alpha_1 = 0$   
 $\alpha_2 = 60$   
 $M_{2p} = .9$   
 $M_{2a} = 1.2$

nozzle

$T_2 = \frac{T_1}{\sqrt{1.5 MN_2^2}} = 1873^\circ R$

$C_2 = MN_2 \sqrt{\lambda R T_2} = 2456 \text{ ft/s}$

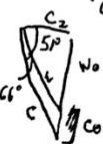
$C_2 = C_1 = \cos \alpha_2 \cdot C_2 = 999 \text{ ft/s}$

$C_0 = \sin \alpha_2 \cdot C_2 = 2244 \text{ ft/s}$

$W_0 = C_0 - U = 1224 \text{ ft/s}$

$W_2 = \sqrt{C_2^2 + W_0^2} = 1580 \text{ ft/s}$

$\beta_2 = \tan^{-1}(\frac{W_0}{C_2}) = 51^\circ$



rotor

$W_0 = -\sqrt{\frac{M_0^2 [C_0^2 + (1-\lambda) W_0^2] - C_2^2}{[1 + (1-\lambda) M_0^2 / 2]}} = -1516 \text{ ft/s}$

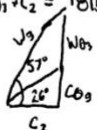
$\beta_2 = \tan^{-1}(\frac{W_0}{C_2}) = -57^\circ$

$C_0 = U + W_0 = -415 \text{ ft/s}$

$\alpha_2 = \tan^{-1}(\frac{C_0}{C_2}) = -26^\circ$

$C_2 = \sqrt{C_0^2 + C_2^2} = 1115 \text{ ft/s}$

$W_3 = \sqrt{W_0^2 + C_2^2} = 1815 \text{ ft/s}$



HPT stage 1

inlet conditions  
 T<sub>2</sub> = 3350 °R  
 A = 12710 RPM = W  
 λ = 1.308  
 R = 1715

design choices  
 $r_{mean} = 14.93 \text{ in}$   
 $\alpha_1 = 0$   
 $\alpha_2 = 70$   
 $M_{2p} = .9$   
 $M_{2a} = 1.2$

nozzle

$T_2 = \frac{T_1}{1.5 \cdot MN_2^2} = 2754^\circ R$

$C_2 = MN_2 \sqrt{\lambda R T_2} = 2978 \text{ ft/s}$

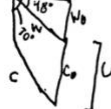
$C_2 = C_1 = \cos \alpha_2 \cdot C_2 = 1018.68 \text{ ft/s}$

$C_0 = \sin \alpha_2 \cdot C_2 = 2798 \text{ ft/s}$

$W_0 = C_0 - U = 1142 \text{ ft/s}$

$W_2 = \sqrt{W_0^2 + C_2^2} = 1530 \text{ ft/s}$

$\beta_2 = \tan^{-1}(\frac{W_0}{C_2}) = 48^\circ$



rotor

$W_0 = -\sqrt{\frac{M_0^2 [C_0^2 + (1-\lambda) W_0^2] - C_2^2}{[1 + (1-\lambda) M_0^2 / 2]}} = -1914 \text{ ft/s}$

$C_0 = W_0 - U = -268$

$W_2 = \sqrt{W_0^2 + C_2^2} = 2168 \text{ ft/s}$

$C_2 = \sqrt{C_0^2 + C_2^2} = 1051 \text{ ft/s}$

$\alpha_2 = \tan^{-1}(\frac{C_0}{C_2}) = -14^\circ$

$\beta_2 = \tan^{-1}(\frac{W_0}{C_2}) = -62^\circ$



APPENDIX B: HAND CALCULATIONS FOR FIRST STAGE VELOCITY TRIANGLES OF TURBOMACHINERY